

Bioinspired Material Approaches to Sensing

By Michael E. McConney, Kyle D. Anderson, Lawrence L. Brott, Rajesh R. Naik, and Vladimir V. Tsukruk*

Bioinspired design is an engineering approach that involves working to understand the design principles and strategies employed by biology in order to benefit the development of engineered systems. From a materials perspective, biology offers an almost limitless source of novel approaches capable of arousing innovation in every aspect of materials, including fabrication, design, and functionality. Here, recent and ongoing work on the study of bioinspired materials for sensing applications is presented. Work presented includes the study of fish flow receptor structures and the subsequent development of similar structures to improve flow sensor performance. The study of spider air-flow receptors and the development of a spider-inspired flexible hair is also discussed. Lastly, the development of flexible membrane based infrared sensors, highly influenced by the fire beetle, is presented, where a pneumatic mechanism and a thermal-expansion stress-mediated buckling-based mechanism are investigated. Other areas that are discussed include novel biological signal filtering mechanisms and reciprocal benefits offered through applying the biology lessons to engineered systems.

1. Introduction

Biologically inspired design is a nontraditional problem solving approach which often results in uniquely engineered solutions for complex practical problems. Furthermore, this approach can often work to catalyze development through the use of a bidirectional approach to problem solving, where both the problem and potential solutions are analyzed simultaneously.^[1] There are many examples of the successful application of bioinspired design: the inch-worm-inspired piezoelectric inchworm motor,^[2] materials capable of legless motion inspired by the anisotropic friction of snake locomotion,^[3,4] inorganic crystallization that mimics the formation of the skeletons of sponges,^[5–7] the ability to defy gravity by walking on walls inspired by the setae of geckos,^[8–10] microlenses inspired by brittlestars,^[11,12] and adhesive materials inspired by mussels.^[13,14]

[*] Prof. V. V. Tsukruk, Dr. M. E. McConney, K. D. Anderson
School of Material Science and Engineering
School of Polymer, Textile and Fiber Engineering
771 Ferst Drive, N.W., Atlanta, GA, 30332-0245 (USA)
E-mail: vladimir@mse.gatech.edu

Dr. L. L. Brott, Dr. R. R. Naik
AFRL/RXBN, Biotechnology Group, Materials and Manufacturing
Directorate
Air Force Research Laboratory
Wright-Patterson Air Force Base, OH, 45433 (USA)

DOI: 10.1002/adfm.200900606

Although there are many examples of success stories involving bioinspired design, the rules and the methods of this approach are still evolving. Nonetheless, it seems quite apparent that the exploration of biological ingenuity and the inspiration of engineering design is a symbiotic relationship. In order to fully leverage this bidirectional approach, it is important to understand the fundamental differences in the approach to problem solving. Generally, Nature's approach is to continuously improve past designs and make changes to solve new challenges; whereas engineers often start their designs literally from the drawing board.^[1] Biology often uses the same tools with small changes for very different roles and these small changes can often provide excellent insight as to the particular specialization of a system.

This article focuses on our recent and ongoing work in the area of bioinspired soft materials for sensing applications. We discuss the role that fish and spiders have played in the inspiration of new material-based approaches to underwater and air-based flow sensing. Research on the fire beetle provided us with the template to develop new infrared sensors and engineered signal transduction. This article also has several underlying themes, specifically material-based signal filtering, Nature's approach to multifunctional receptor materials, and the symbiotic relationship between engineers and biologists.

2. Underwater Flow Sensing

One such system designed through the principles of bioinspiration is the mechanical flow sensor, which is designed to mimic a fish's ability to detect and track fluid flow. Flow measurement is a basic area of measurement, capable of utilizing many different physical relationships.^[15,16] Although measuring flow velocity is a straightforward process, flow visualization (velocity, pressure, and vorticity fields) is not nearly as simple. Typically, hydrodynamic visualization is used for experimental fluid dynamics studies, but there are many other applications including navigation and obstacle avoidance of autonomous underwater vehicles, underwater surveillance, seismic monitoring of tsunamis, oceanographic studies, mine reconnaissance, pollution monitoring, drag-minimization of submarines, passive sonar, and wake-following.^[17,18]

An in-depth description of flow-visualization is beyond the scope of this paper and can be found in relevant reviews.^[19,20]

From a practical viewpoint, there is a large demand for a compact flow-visualization system that is capable of acting as a passive detection system for a variety of application including guidance of autonomous underwater vehicles (AUVs). This involves developing both a suitable flow visualization system and signal-processing techniques to make use of the data that is collected. The underwater flow visualization system is part of an on-going effort to develop high sensitivity devices composed of arrays of mechanical-based flow sensors. A major advantage over this technique compared to more common bulk-based (free-flow) techniques, such as Doppler shift, is its highly passive and portable nature. A major disadvantage is that the sensing takes place near the stagnant boundary layer of the surface, which significantly increases the need for very sensitive sensors that do not interfere substantially with the flowing environment.

Here, we focus on various types of flow receptors and the application of knowledge gained from biology to guide new materials-based approaches to fluid and air flow sensing. The work highlighted here serves as a simple, yet effective demonstration of the capability for bioinspired design to solve difficult engineering challenges through the study of solutions that nature has provided. We have focused our investigation of flow sensing from the perspective of creating material-based, sensitivity-enhancing strategies.

The hair-like flow sensors discussed in these studies were developed and fabricated over several years.^[21–24] Sensors of this type developed in the Liu group are mechanical-based piezoresistive hairs that were inspired by fish lateral-line flow receptors (Fig. 1). The hair sensors consist of a polymer hair on a silicon-based microcantilever with a gold circuit patterned on the silicon surface (Fig. 1B). The whole sensor is covered in parylene, which acts as a waterproof coating on the sensor because it is a pin-hole free dielectric layer.

The tall polymer hair on the sensors absorbs mechanical energy from the surrounding water flow, which is transmitted to the piezoresistive cantilever, which bends in response to the transmitted mechanical stress. The flow-derived signal is

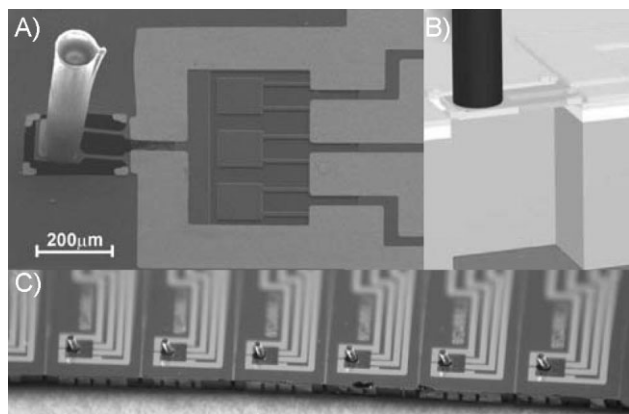


Figure 1. Microfabricated flow hair sensor: A) SEM image of pre-existing flow sensors. B) Schematic of flow sensor. C) A photograph of an array of flow sensors. Adapted with permission from Reference [21]. Copyright 2007, IEEE.



Michael E. McConney received his B.S.E. degree in Chemical Engineering in 2004 from the University of Iowa. He received his Ph.D. in Polymer Materials Science and Engineering at Georgia Institute of Technology in July 2009 and has accepted a post-doctoral position at Air Force Research Laboratory in Dayton, OH starting fall 2009. He has co-authored

more than 15 refereed publications and made more 10 oral and poster presentations at National Conferences. His current research interests include chemical sensing, liquid-crystal elastomers, and bioinspired optical materials.



Vladimir V. Tsukruk received his M.S. degree in Physics in 1978 from the National University of Ukraine and his Ph.D. and D.Sc. in Chemistry in 1983 and 1988 from the National Academy of Sciences of Ukraine, and was a post-doc at U. Marburg, T. U. Darmstadt, and U. Akron. Currently, he holds a joint appointment as a Professor at the School of

Materials Science and Engineering and School of Polymer, Fiber, and Textile Engineering, Georgia Institute of Technology, Director of Microanalysis Center, and a co-Director of BIONIC Center. He has co-authored around 300 refereed journal articles and 4 books. His research interests are in the fields of surfaces, interfaces, molecular assembly, and nano- and bioinspired nanostructures and nanomaterials.

transduced through a bending-induced resistance change. These sensors, in an original design, have a minimum detection threshold of above 0.2 mm s^{-1} .^[21] Maximizing the sensitivity and minimizing the detection threshold by different means are very important for many practical reasons, including enhancing the sight range of the system and increasing the spacing of a sensor grid. These features must be combined with a signal-processing system that is capable of handling input from a multihair array.

2.1. Flow Reception in Fish

Fish rely on flow receptors for several important tasks, including navigating, hunting prey, rheotaxis, and schooling. Fish have developed the ability to sense flow rates in water with velocities as low as several micrometers per second.^[25,26] The lateral line is a

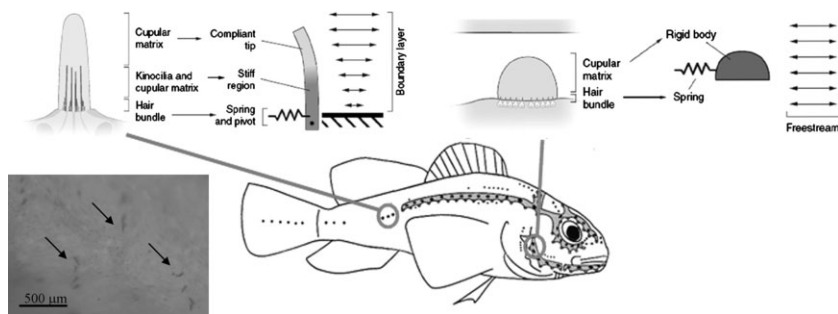


Figure 2. A schematic of the different components making up the fish flow sensing lateral line system. Top left: Superficial neuromasts are situated on the outside surface of the fish and undergo a bending deformation. Bottom left inset: An optical fluorescence image of goldfish superficial cupulae. Top right: Canal neuromasts are below the surface of the fish in tunnels and depressions. Adapted with permission from References [18, 29]. Copyright 2006 The National Academy of Sciences and 2007 The Company of Biologists, respectively.

system of flow-transducing neuromasts located along the outside of the fish body and also inside a series of pores/canals along the body of the fish; called superficial neuromasts and canal neuromasts, respectively (Fig. 2). A neuromast typically includes from 20 to 1000 mechanosensing hair cells.^[27] Neuromasts, the basic flow-sensing unit in fish, are made up of many mechanosensing hair cells covered by a single, compliant bio-hydrogel structure called a cupula (Fig. 2).^[28,29] In some species, the cupula is supported by interior fibrils. It is established that superficial neuromasts are more sensitive to flow velocity (0 Hz (DC)–50 Hz), whereas the canal neuromasts are more sensitive to acceleration (50–400 Hz range).^[30–32]

The hair cells in fish neuromasts contain a single long hair called the kinocilium, and a series of shorter hairs cells, stereovilli (Fig. 3).^[33] The kinocilium acts to support the hair bundle and transmit stimuli while exerting an opposing force on the hair bundle in response to stimuli. It also acts as a component of the

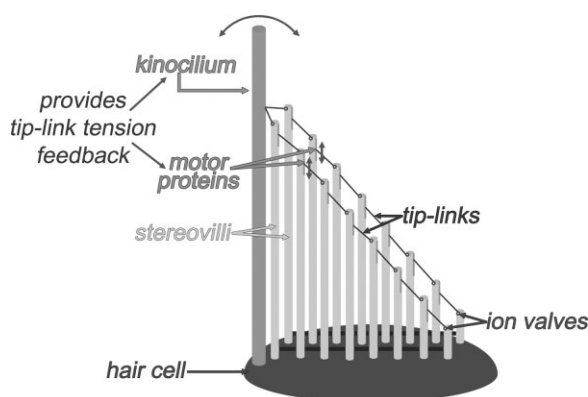


Figure 3. A schematic of a hair cell (kinocilium not to scale). The kinocilium provides the stereovilli with support and is capable of bending in response to saturating stimuli to maintain the sensitivity. In response to mechanical stimuli the stereovilli with deform, which changes the tension on the tip-links, which thereby changes the rate of neuron firing because the ion-valve position changed. Furthermore, there are motor proteins connected to the tip-links, which are capable of reacting to the tension.

feedback mechanism, which keeps the cell sensitive to minute stimuli while preventing signal saturation from large stimuli.

The stereovilli are small, cellular protrusions occurring in bundles. Their tips are connected via protein linkages to a mechanically gated ion channel.^[34] The tip-linkage acts to transmit mechanical stimuli to the ion channel, which opens in response to stress. Upon opening, ions pass into the cell, thereby setting off an action potential. A motor protein allows the linkage point along the stereovilli to change, which is also a component of the cellular feedback mechanism.^[35] A full discussion of the details regarding hair-cell's sensing approach and capabilities can be found in recent reviews.^[36–41]

Cupulae are usually around 100–1000 μm long, but their size and properties have been shown to vary greatly for different species.^[42] These cupulae couple the mechanosensing hair cells to the surrounding water flow by increasing the drag of the neuromasts, thereby enhancing the signal transmission to the hair cells. These cupula enhance the drag of the neuromast in several ways, including increasing the overall surface area of the neuromast. The hydrophilicity and the permeability of the hydrogel-like material that makes up the cupula may also enhance the signal absorption through an enhanced friction factor associated with the material. As mentioned above, the superficial neuromasts are more sensitive to flow velocity and the canal neuromasts are more sensitive to acceleration.^[30–32] The signal filtering of these receptors is controlled by several factors including the location of the receptors and the shape of the cupula.^[43]

Some fish, such as blind cave fish, have cupulae with embedded fibers in their superficial neuromasts (Fig. 4). It is not immediately clear why some fish have these cupular fibers and others do not. It is believed that these cupular fibers function as a structural support network for the cupula, allowing the cupula to grow to greater distances away from the stagnant boundary layer of the surface of

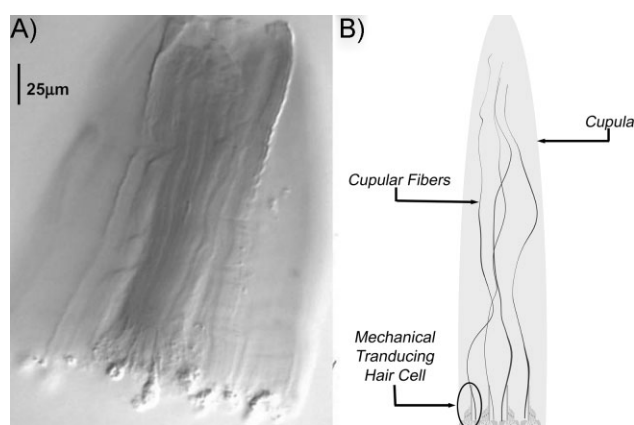


Figure 4. A) Blind cave fish superficial neuromast, notice the cupular fibers running the length of the cupula. B) A schematic of a blind cave fish superficial neuromast. Adapted with permission from Reference [53]. Copyright Elsevier 2008.

the fish. These fibers may also aid in coupling the hair cells to the hydrogel cupula, which plays a role in transmitting the energy from cupula to the hair cells.^[42,44,45]

2.2. Fish Cupula Material Studies

The purpose of this study was to guide development of a novel approach to improve the performance of microfabricated flow hair sensors introduced by the Liu group (Fig. 1). As stated above, the cupula and support fibers are specialized structures that enhance flow sensing properties of hair cells. Therefore, we set out to create specialized structures to efficiently transmit flow energy to the sensors. In order to guide the development of an artificial cupula, the mechanical properties of superficial cupula in blind cave fish were characterized.

To this end, the mechanical properties of blind cave fish cupulae were directly measured using fluid-based surface force spectroscopy with a colloidal probe. The elastic modulus of the fish cupula was measured in water using atomic force microscopy (AFM) in force-volume mode in accordance with usual approach developed in our group (Fig. 5).^[46–48] The loading plot in coordinate of penetration^{3/2} versus the applied load (Hertzian coordinate plot) was observed to be highly nonlinear (Fig. 6). For purely elastic solids, it is expected to be linear. The nonlinear response is generally caused by viscoelasticity of the materials associated with a time-dependent, viscous response.^[49,50]

The maximum applied load was extremely low, on the order of 250 pN, which is significantly less than the force needed to break a single C–C bond (on the order of several nN). Therefore, any nonlinearity of the Hertzian coordinate plot is not due to plastic

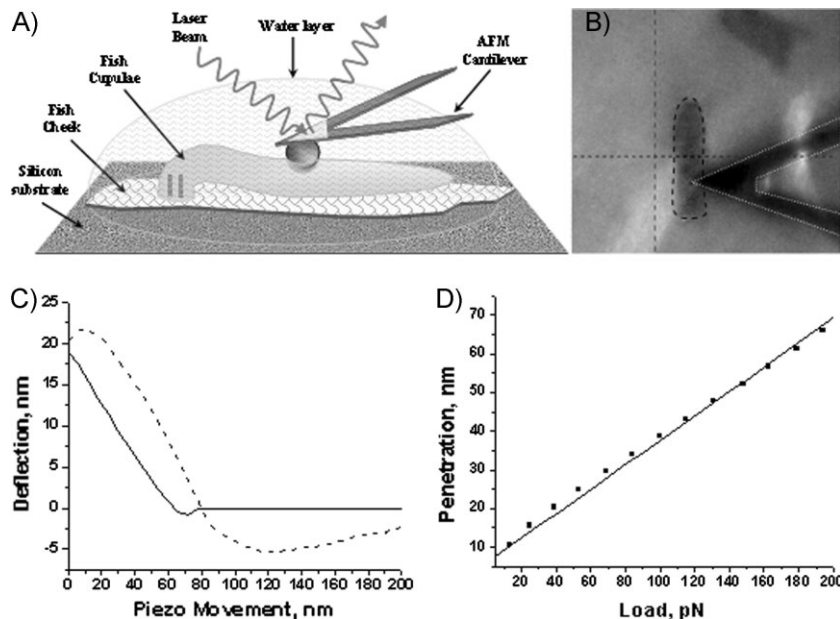


Figure 5. A) Schematic of setup for the cupula property measurements. B) An optical image of the cantilever pressing on a stained cupula. C) A typical force distance curve from fish cupula. D) A typical force-penetration curve from a fish cupula. Adapted with permission from Reference [51].

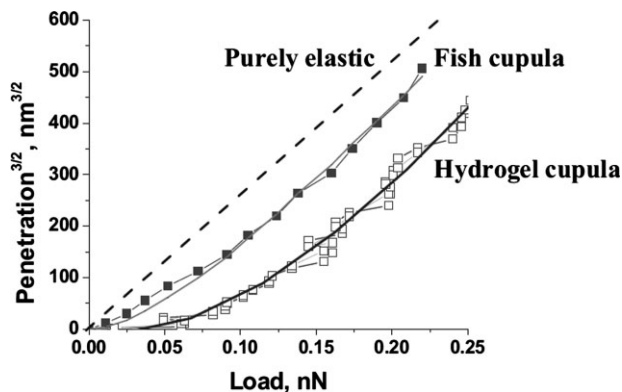


Figure 6. A Hertzian coordinates plot, load-penetration^{3/2} curve comparing the non-linear mechanical response of the fish cupula to the PEG cupula. Reproduced with permission from Reference [51].

deformation. The Voight viscoelastic model was combined with the Hertzian contact model to fit the nonlinear loading data for the cupula. The bio-hydrogel was measured to have an elastic modulus of 9 kPa and a relaxation time of 0.42 s, which are both characteristic of compliant and viscous materials.^[51]

2.3. Fish-Inspired Artificial Cupula

2.3.1. Development of Artificial Cupula Material

The synthetic cupulae with comparable mechanical properties were fabricated by photo-crosslinking tetra-acrylate functionalized poly(ethylene oxide) glycol (PEG) (Fig. 7).^[51] The initiator used to crosslink the acrylate-functionalized PEG was 2,2-dimethoxy-2-phenylacetophenone dissolved in 1-vinyl-2-pyrrolidone.^[52] The PEG was deposited directly on the hair sensor and then exposed to UV light at 365 nm under varying intensities and times, as described in detail elsewhere (Fig. 7).^[51,53] Photomasks were used to localized crosslinking and thereby pattern the PEG into different shapes through selective exposure of the hydrogel.

The Voight viscoelastic model combined with the Hertzian contact model was used to fit the nonlinear experimental loading data obtained by colloidal probe spectroscopy on top of the synthetic cupula (Fig. 6). This approach, when applied to the synthetic cupula with intermediate molecular weight between crosslinks, resulted in an elastic modulus of 9.5 kPa and a relaxation time of 0.5 s, fairly close to results obtained previously for biological cupulae (Fig. 6).^[51]

2.3.2. Sensing Performance of Artificial Cupula

The bioinspired approach was quantified by testing the hair sensors before and after the hydrogel had been applied to the hair sensors.

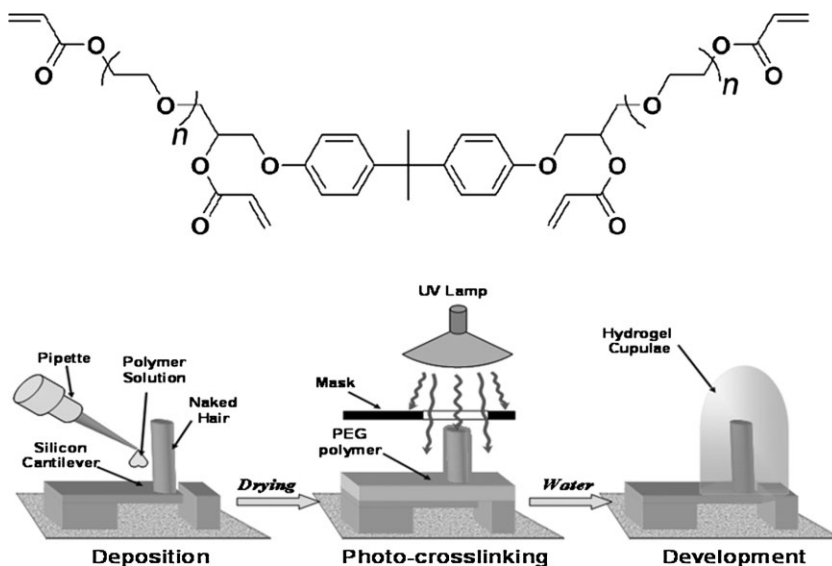


Figure 7. Top: a schematic of the photo-crosslinkable acrylate-functionalized PEG used to fabricate the artificial cupula. Bottom: a schematic diagram of the fabrication process leading to dome-like cupulae. Adapted with permission from Reference [51].

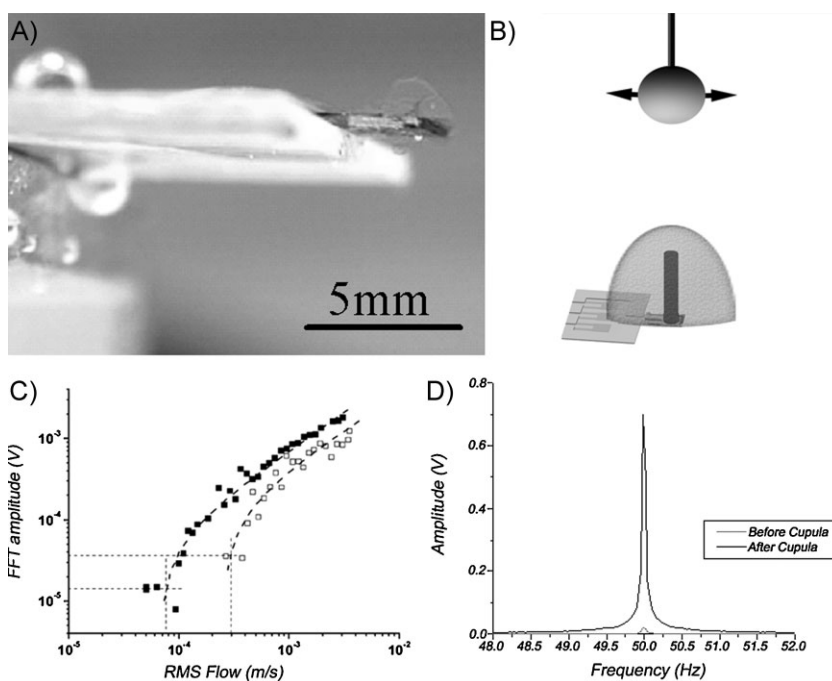


Figure 8. Dome-shape cupula sensitivity measurements. A) Optical image of a sensor encapsulated in a dome-shaped cupula. B) Schematic of AC test setup. C) Response versus frequency at 50 Hz excitation frequency before sensor modification and after sensor modification. D) Signal response versus velocity at 50 Hz (open before cupula, solid after cupula modification). Adapted with permission from Reference [51].

The flow-sensor testing was carried out underwater by shaking a dipole placed at set distances from the sensor surface (Fig. 8). The dipole amplitude and frequency were controlled and monitored, while simultaneously monitoring the Fourier transform of the sensor piezoresistive output. This standard dipole test allows for prediction of the water velocity ($v \approx 1/r^3$) at the sensor surface

based on the frequency of the dipole, the amplitude of the dipole, and the dipole–sensor distance. The dipole amplitude was varied to obtain the sensitivity. Minimum threshold stimuli were measured by lowering the dipole amplitude until the sensor output became erratic. A second test involved constant (DC) laminar flow over the sensors in a flow chamber. In this test the flow velocity was varied controllably and the sensor piezoresistive output was simultaneously monitored.

After the measurements were performed on the initial sensor with a bare hair, the sensor was encapsulated in a dome-shaped cupula and tested under identical flow conditions. The unaltered sensors tested here had minimum water velocity detection thresholds of around 0.2 mm s^{-1} . After the synthetic cupula was applied to the sensors, the threshold velocities improved by over 2.5 times to roughly 0.075 mm s^{-1} (Fig. 8). In the linear regime of the sensor output, the sensitivity increased by 60%, going from $4.3 \text{ mV}/(\text{mm/s})$ to $6.8 \text{ mV}/(\text{mm/s})$. Surprisingly, the application of the cupula resulted in sensors with a lower noise floor, decreasing from about $35 \mu\text{V}$ to about $10 \mu\text{V}$, and dynamic range increased by half an order of magnitude. This result indicates that the inertia-based dome-shaped cupula might also have a signal filtering role, with random noise being suppressed by the viscously coupled cupula. The sensitivity improvement led to very significant sensor output enhancement at relatively higher root-mean-square (RMS) flow rates (Fig. 8). The DC measurements resulted in a fourfold improvement in both the sensitivity and minimum threshold stimulus as discussed in the original paper.^[51]

Theoretical estimations indicated that the expected signal amplification for the increased cross-sectional area accounted for only about half of the actual signal amplification, indicating additional contributions to the signal absorption. It is quite reasonable to conclude that the enhanced friction factor associated with the cupula, which is composed of 90% water, is related to the inherent permeability properties of the hydrogel. The enhanced friction associated with the inherent materials can be related to the material's hydrophilicity, as well as friction associated with mechanical coupling between the flowing water and the water inside

the porous swollen hydrogel.^[54] Further details regarding experimental procedure, results, and interpretation are available in a prior publication.^[51]

These results indicated that this bioinspired approach of mimicking the fish receptor superstructure is promising. Although significant improvements were seen with the addition

of the bioinspired material, further improvements are needed to enhance the capabilities and ensure the viability of a flow-visualization system. The dome-shaped synthetic cupulae introduced above are an important biomimetic design for canal-based sensing. The tall superficial cupula is the appropriate biological analogue of the other type of flow sensing, as discussed below (Fig. 2).

2.3.3. High-Aspect Artificial Cupulae

The focus of this development was to build on previous demonstrations of improvements to engineered hair sensors from bioinspired support structures. Specifically, the aim was to improve the previous dome-like cupula's performance by fabricating a higher-aspect ratio cupula, much like that of fish superficial cupula. The dimensions and aspect ratio of the blind cave fish superficial cupulae chosen for bioinspiration were measured using confocal fluorescence microscopy and conventional optical microscopy (Figs. 2 and 4). The superficial cupulae were measured to have an average height of $(104 \pm 13) \mu\text{m}$, a width of $(26 \pm 3) \mu\text{m}$, and thus an aspect ratio of 4.0 ± 0.8 . We used this aspect ratio as a general guide for the development of high-aspect ratio synthetic cupula.

In order to fabricate tall synthetic cupula with a shape like that of superficial cupulae of fish (flaglike), we developed a controlled drop-casting method.^[55] To facilitate this endeavor, a 3-axis micropositioner was used in conjunction with a side-view camera to position a syringe filled with the PEG macromonomer solution directly above the hair of the sensor (Fig. 9). Several drops of PEG solution were precisely dropped onto the hair without wetting the base surface (Fig. 9). This method provided a degree of control over the height and width of the cupula by controlling the number of drops and the volume of each drop, respectively. Furthermore, cupula collapse was prevented by avoiding wetting the surface surrounding the sensor. The hydrogel was then swollen in deionized (Nanopure) water (Fig. 9C).

A recent study indicated that fish bio-hydrogel cupula material was softer (elastic modulus $E \approx 10^5 \text{ Pa}$)^[29] than our blind cave fish measurements and that the stiffer cupula of blind cave fish was due to their rather dense network of cupular fibrils. Therefore, for these studies, we used crosslinking conditions that better matched the fish cupula's inherent properties instead of the properties of the blind cave fish composite cupula.

The performance of the higher aspect ratio synthetic cupula as a sensing enhancement structure was tested in a similar manner as the dome-shaped cupula, using the standard dipole test (Fig. 8B). There was an impressive difference in sensor performance before and after the addition of the bioinspired structure. The flow sensitivity improved by 38 times, going from $3.2 \text{ mV}/(\text{mm}/\text{s})$ to $122 \text{ mV}/(\text{mm}/\text{s})$, whereas the sensors capped by the dome-shaped cupula had a sensitivity of $6.8 \text{ mV}/(\text{mm}/\text{s})$, 60% higher than the unaltered sensor (Fig. 10).

Therefore, the sensitivity improvement was over 60 times more for the high-aspect ratio cupula, a tremendous improvement (Fig. 10). The high-aspect ratio cupula improved the sensor minimum detectable velocity from $100 \mu\text{m s}^{-1}$ to $2.5 \mu\text{m s}^{-1}$. Whereas, the dome-shaped cupula resulted in a minimum threshold velocity of $75 \mu\text{m s}^{-1}$. Overall, the minimum detection threshold improvement of the high aspect ratio cupula out-

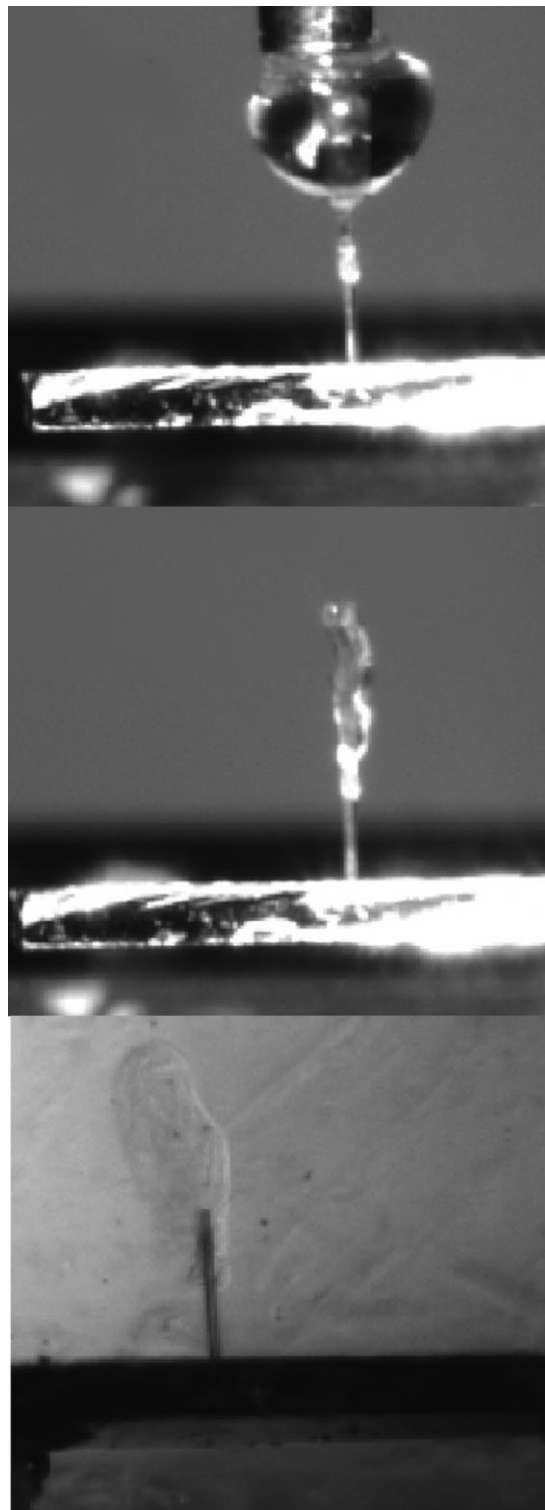


Figure 9. Optical pictures of the formation of the high-aspect artificial cupula. Top: formation of the tall cupula involves precisely placing a droplet on top of the hair sensor, concentrating the polymer solution via evaporation, and finally followed by polymer adsorption. Middle: after repeating this process a high-aspect ratio PEG structure is formed. Bottom: upon crosslinking and swelling, the formed cupula generally maintains the high-aspect shape.

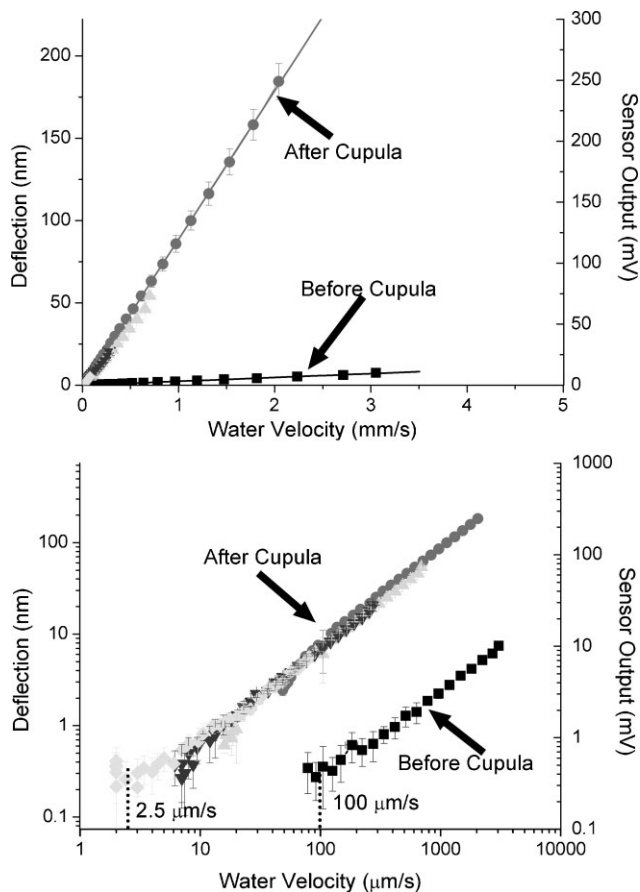


Figure 10. Top: the results of the dipole test plotted on a linear scale, showing an improvement in the sensitivity of 40 times after adding cupula. Bottom: the results of the dipole test plotted on a log–log scale, showing an improvement in the threshold deflection of 40 times. Top and bottom: squares: “bare” sensor response at 15 mm distance from the dipole; circles, up triangles, down triangles, diamonds: sensor response with cupula, 15 mm, 22 mm, 30 mm, 45 mm distances from the dipole, respectively. Reproduced with permission from Reference [55]. Copyright the Royal Society of Chemistry 2009.

performed the dome shape by 15 times. It is interesting to note that the more compliant high aspect ratio cupula did not result in a lower noise floor, as the dome-shaped cupula did.

The achievement of an overall minimum detectable flow of $2.5 \mu\text{m s}^{-1}$ is quite remarkable considering limits of initial bare hair sensors within $0.1\text{--}0.2 \text{ mm s}^{-1}$. Furthermore, it is even lower than the minimum detectable flows of $18\text{--}38 \mu\text{m s}^{-1}$ that have been measured in different fish.^[25,26,56] Therefore, through the bioinspired approach of fabricated sensor super-structures with similar shape and properties, we were able to truly rival the performance of our biological models. This work serves as a strong, yet simple, example of the powerful capabilities that bioinspired design has to offer for rational engineering sensory structures.

2.3.4. Fabrication of Cupular Fibrils

As was mentioned above, the superficial cupula of blind cave fish is a composite structure composed of a very compliant bio-hydrogel

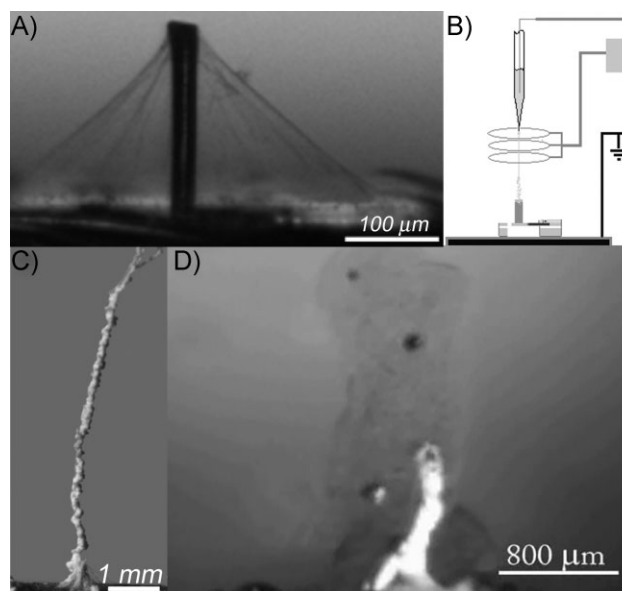


Figure 11. Electrospinning. A) The result of conventional electrospinning. B) A schematic of the focused electrospinning setup used to produce long-fibrils. C) An optical image demonstrating how high the fibrils can be grown from the hair, notice the scale differences in A and C. D) A tall artificial cupula encapsulating a hair with electrospun fibrils. Reproduced with permission from Reference [53]. Copyright Elsevier 2008.

supported by a relatively dense network of long fibrils. In order to further leverage our bioinspired cupula, we adapted an electrospinning technique to fabricate tall micro/nanofibrillar structures on top of the hair sensor. An in-depth review of electrospinning is beyond the scope of this article, but one may refer to relevant papers.^[57–60]

These fibrils were electrospun from a solution of polycaprolactone dissolved in acetone (17.5%). In electrospinning, a high voltage potential forces a polymer solution from a capillary to a collecting plate.^[61,62] In this case the polymer hair was sitting on the grounded collection plate and was being targeted for the fiber deposition. The challenge with this process was in harnessing the random nature of the fiber formation and directing the polymer to form coherently on and around the hair cell sensor (Fig. 11).^[53] To direct the fibers, a copper focusing ring was placed between the capillary and the haircell (Fig. 11).^[63] The ring was biased with the same charge as the polymer solution. This allowed the height of the fiber to be built up into a tall freestanding fibril structure as high as 10 mm (Fig. 11).^[53] Nonetheless, excessive fiber heights (exceeding 1–2 mm) do not support the hydrogel cupula and therefore for cupular support structures the fibrils are kept at moderate heights.

Upon fiber formation, the PEG hydrogel could be placed over the fiber-hair structure and cured as discussed above. The combined structures were able to support hydrogels with significantly increased height (aspect ratio within 5–10 times).^[53] Overall, we were able to increase the height of the hydrogel cupula by about three-fold, compared to the unsupported hydrogels, by using the electrospun fibers for support (Fig. 11). By using the spun fiber as support to increase the height of the hair cell and the overall aspect ratio of the hydrogel cupula system, we can expect to

see even further leveraging of our bioinspired approach to obtain further sensitivity gains.

3. Air Flow and Vibration Sensing

Now, we shift our focus to another type of hair sensor for air-flow sensing. This technology has been used in many applications ranging from simple examples such as a wind sock to indicate the direction of air movement to the Pitot tube to measure the airspeed of an aircraft. Additionally, mass-flow sensors can be used to quantify the amount of gas entering a given area. Nature also makes use of the air-flow sensor, but on a much smaller scale and with high sensitivity.^[64] Mimicking these small and precise systems may allow for the construction of many smaller and automated aircraft which are capable of responding to changes in air flow based on direction and velocity.^[65] Such a system could also lead to a better understanding of close proximity navigation as seen in swarms of birds and insects.

3.1. Air Flow and Vibration Sensing in Spiders

Wandering spiders (*Cupiennius*) are a genus that, unlike most spiders, do not use webs for hunting.^[66] Instead, wandering spiders hunt through a more conventional approach, by waiting motionless until prey is close, then they attack, reacting in 200–700 ms to capture and bite their prey.^[66] The larger species are capable of preying upon small frogs and lizards. Their hunting strategy relies heavily upon their highly evolved vibration sensing receptors and wind-sensing receptors. Barth's work with these creatures has revealed many unique and amazing features about their sensing, which is a very fruitful source of inspiration.^[66] Despite their strong dependence on their high vibration and wind-sensing ability, wandering spiders have relatively simple nervous systems with brains that have roughly three times less neurons than the migratory locust and almost nine times less than the honey bee.^[66] Therefore, understanding the ability of the wandering spider to efficiently process information may inspire novel solutions to signal processing challenges associated with large arrays of sensors.

3.1.1. Air-Flow Sensing in Spiders

Highly sensitive trichobothria air-flow receptors are a major asset to these spiders for sensing their vibrational environment (Fig. 12). Many spiders have trichobothria, but the *Cupiennius salei* has by far the most, with over 900 counted. These hair (sensilla) receptors are found on the legs and pedipalps of the spider.^[67] The resonance ranges from 40–600 Hz, depending on the length of the hair rather than the mass.^[68,69] Often the hairs are arranged in relatively tight groupings, which are made up of hairs of differing lengths, ranging from 100–1400 μm (Fig. 12). These associated hairs of varying lengths are able to act as band-pass filters through utilizing the stagnant boundary layer at the surface of the spider leg.^[70]

The hair receptors have a hairs-on-hair morphology that increases the surface area (drag) to mass (inertia) ratio of the hair, thereby increasing the coupling between the hair and the flowing air (Fig. 12). Instead of bending, the hair shaft responds to

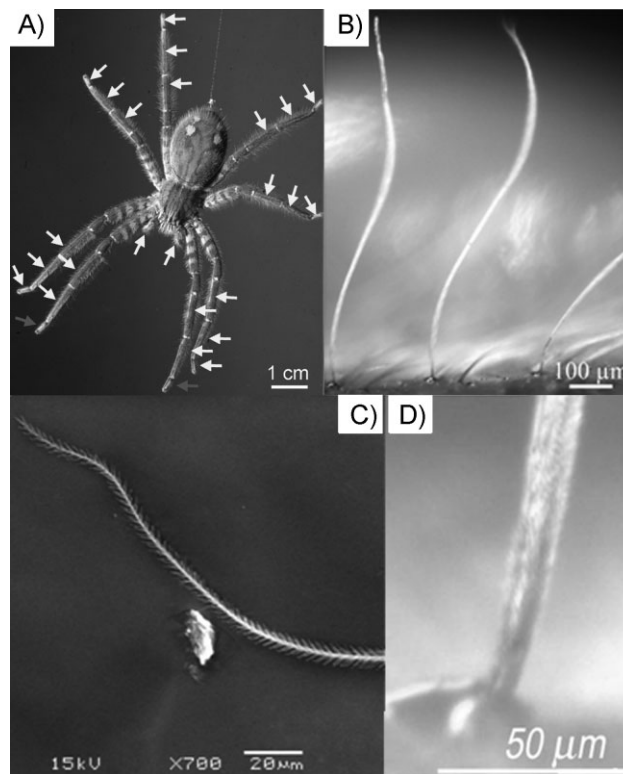


Figure 12. A) *Cupiennius Salei* with trichobothria locations indicated with arrows, arrows indicate the location of hair receptors shown in (B). B) An optical micrograph of trichobothria on the pedipalp. C) Optical micrograph of the socket of a trichobothria. D) An SEM micrograph of a trichobothria, notice the hairs-on-hair morphology of the hairs, which acts to enhance signal absorption through enhanced drag. Reproduced with permission from Reference [75]. Copyright the Royal Society of Chemistry 2009.

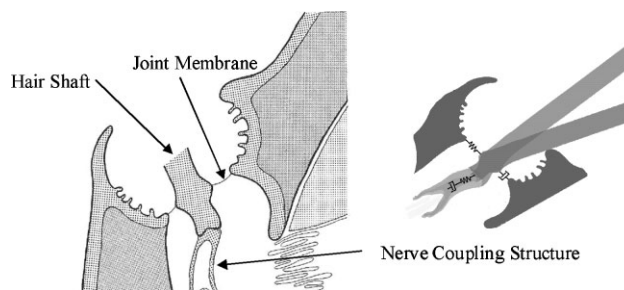


Figure 13. Right: schematic of the functional physiology of Trichobothria in Wandering spiders. Left: a schematic indicating the viscoelastic nature of the hair receptor's response and the unknown location of the time dependant properties. Adapted with permission from Reference [66]. Copyright 2002, Springer-Verlag.

air-stimulus by pivoting about a supporting membrane. The pivoting hair transduces air flow by deforming the nerve through a nerve coupling structure near the pivoting axis (Fig. 13).

In-depth fluid dynamics simulations have calculated that the trichobothria have a torsional constant on the order of 10^{-11} to 10^{-12} N m rad^{-1} . Furthermore, these simulations predicted a slight time dependency of the hair response, which was quantified

with a damping constant on the 10^{-14} N m s rad $^{-1}$.^[71] Insect and arthropod mechanoreceptors will produce an action potential at deflections on the order of 1 nm.^[72] This combination of high flexibility and low threshold deflection makes for an extremely sensitive flow receptor. In fact, trichobothria are some of Nature's most sensitive receptors with threshold stimuli estimated to be 10^{-20} to 10^{-19} J, an extremely low value.^[67] It is important to note that minimum threshold deflection measurements indicate a high-pass nature at very low frequencies, approaching DC. Specifically, the minimum deflection needed to elicit a response from the trichobothria roughly doubles from 100 Hz to 10 Hz, independent of the length of the hair.^[73]

3.1.2. Measuring the Mechanical Properties of Trichobothria

In a previous study, we investigated a high-pass behavior in vibration-sensing slit receptors by performing AFM-based force spectroscopy on an associated pad material that acts as a mechanical signal transmitter. We found that the pad's elastic modulus steeply increased with frequencies above 10 Hz, which made the pad a good stress transmitter at high frequencies and a good stress absorber at low frequencies.^[74] The elastic modulus data correlated well with the nerve response data, which provided strong evidence that the pad material was acting as a viscoelastic mechanical stimulus filter. To our knowledge, this was the first evidence of viscoelastic mechanical filtering in biology.

The main focus of this study was to directly measure the mechanical properties of the trichobothria. Furthermore, we were interested in investigating the origin of the high-pass behavior seen at low frequencies in the nervous response data. We directly characterized the mechanical response of the air-flow receptors using force-spectroscopy (Fig. 14).^[75] The tests were performed by landing an AFM probe on a trichobothria of a live wandering spider. As mentioned, these hairs behave like spring-loaded levers; the stiff hair shaft does not bend (Fig. 13).

The measurements were dependent on two critical assumptions, that no hair-shaft bending occurred and the probe tip did not penetrate into the hair shaft. Each assumption was verified. Indeed, a linear increase of hair deflection was seen at all distances for the range of applied forces and the stiffness followed a slight square relationship with distance. This confirmed that the hair was deflected rather than bent. To verify that no indentation was occurring in the hair, independent force measurements were done on an immobilized hair that had been removed from the spider and secured to a silicon substrate. Since only modest normal loads were used, the indentation depth was close to the experimental uncertainty and could therefore be discounted. The penetration did not exceed 1 nm for the applied loads and thus did not interfere with measurements.

The force-spectroscopy measurements indicated that the response of the trichobothria had strong frequency dependence, thus far not observed for these receptors. Specifically, sensilla deflection per unit of applied force increased strongly as the frequency dropped below 10 Hz. Although, the strong dependence was surprising, it is not surprising that it was not previously observed because the past fluid dynamics experiments measurements were performed at frequencies of 10–1000 Hz, just above the strong dependent behavior. Nonetheless, the torsional constants were measured to be on the order of 10^{-11} N m rad $^{-1}$,

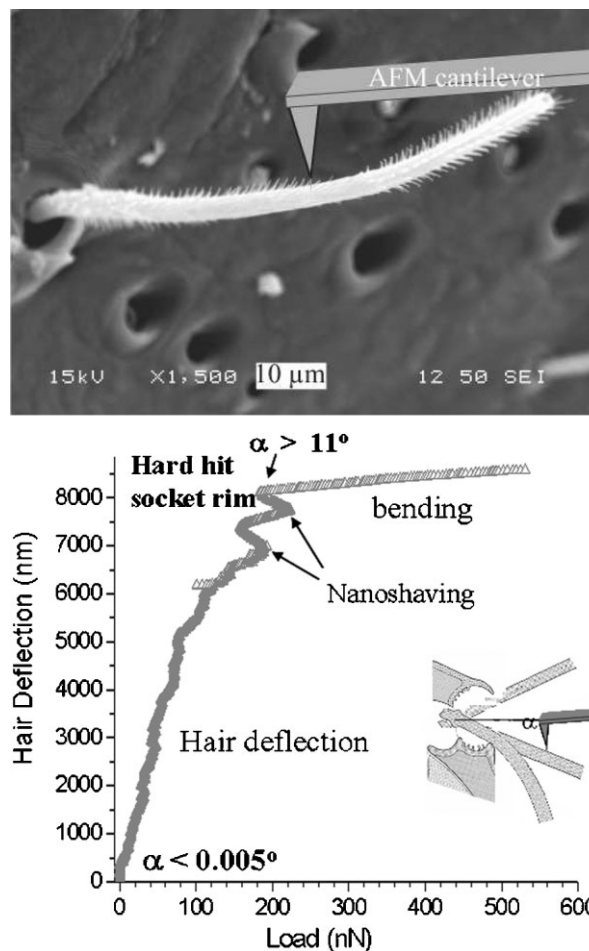


Figure 14. Top: an SEM of a trichobothria with a schematic cantilever added indicating the measurement methodology. Notice the hairs-on-hair morphology has been shaved off. Bottom: a large scale load-deflection curve that shows the pivoting response of the receptors, until it finally reaches the socket edge, at which point it bends. Reproduced with permission from Reference [75]. Copyright the Royal Society of Chemistry 2009.

which is in good agreement with past work involving fluid dynamics. Furthermore, data fit from higher frequencies produced damping constants on the order of 10^{-14} N m s rad $^{-1}$. In order to properly fit the data over the experimental frequency range, a 3-parameter model was utilized, which consists of a spring-element in parallel with a spring and dash-pot element that is in series.

The higher than expected damping constant indicates a viscoelastic component in the receptor structure. It was suggested that the time-dependant dash-pot element was either the structure, or the haemolymph filled region surrounding the nerve-coupling structure, or the nerve coupling structure itself (Fig. 13). Without measuring the mechanical properties of the individual components, it is not possible to decisively determine the origin of the viscoelastic behavior. Nonetheless, the implications of the different scenarios can be qualitatively interpreted and can be translated into implications for engineered sensors for leveraging. Depending on whether the frequency stiffening component acts to

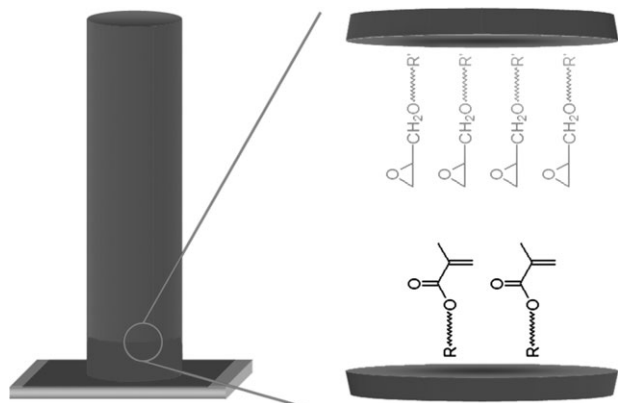


Figure 15. Schematic of the two-tiered spider-inspired pivoting hair structure, the green region depicts the glassy SU-8 epoxy photoresist and the blue region depicts the rubbery photoresist. The zoomed region depicts the interfacial grafting.

transmit mechanical energy or not determines whether the component will act in a high-pass or a low-pass role, respectively.

3.1.3. Spider Inspired Sensing Structures

As mentioned the flow-sensing spider hairs do not bend, but instead pivot about an axis supported by a flexible membrane (Fig. 13). Furthermore, we demonstrated that spider air-flow receptors have a time-dependent response. Also, our past investigation provided strong support that spiders use viscoelastic materials to filter mechanical stimuli in strain receptors to maximize response in certain frequency range.

Considering the design above, we fabricated an upgraded two-tier hair for cantilever based sensors composed of a two-level hair, a stiff polymer hair built upon very compliant rubbery support firmly grafted to the substrate (Fig. 15). Construction of such an artificial hair with tailored mechanical properties was accomplished through the development of a tailored photoresist system thereby leading to the two-tiered hairs with inherently viscoelastic behavior provided by the rubbery attachment.

Construction of the hybrid haircell began by applying an adhesion promoter, 3-(trimethoxysilyl)propyl methacrylate, to the cantilever substrate. This monolayer provides a covalent bond between the silicon surface and the flexible, bottom section of the haircell. The formulation for the rubbery photoresist is based on a poly(butadiene)-dimethacrylate combined with a type 1 photoinitiator. To improve the adhesion between the two layers of the haircell, a small amount of glycidyl-methacrylate was also added to the formulation. This custom photoresist can be patterned, cured, and developed using the same techniques as commercial photoresists. Once the lower section of the haircell was made, a glassy photoresist, SU-8, was patterned directly on top of the existing rubbery section. In all, the overall height of a typical haircell was approximately 800 μm tall, with the rubbery section being 80 μm tall (Fig. 16).

The completed haircell is robust, flexible, and resistant to acids, bases, and various solvents. The durability of these multilayered haircells is impressive and can withstand over 1000 bending cycles with mechanical deformation performed with a mechanical profilometer with hair bending of almost 90° and returning to their initial vertical orientation (Fig. 16). Additionally, the use of

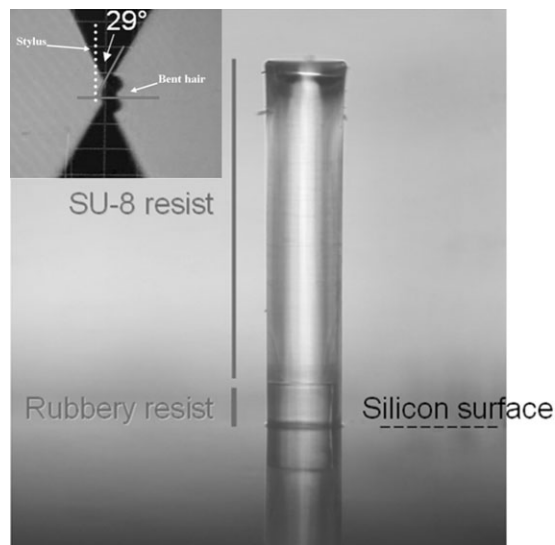


Figure 16. An optical image of a fabricated two-tiered hair. The inset is an optical image of a profiler stylus bending a two-tiered hair attached to a silicon substrate. The hair was able to withstand over 1000 of such bending cycles.

adhesion promoters was validated since the interface bonds were shown to be stronger than the hairs themselves. Once completed, the entire sensor was covered with a parylene-A coating to provide a conformal, pinhole-free protective layer over the entire device.

The question of the location of the time-dependent component in the spider receptor leads us to imagine even more advanced designs. An even further development could be suggested with the addition of a viscoelastic material in place of the silicon in the cantilever. Such a design could lead to sensors with inherent band-pass capabilities. At frequencies deemed too low, mechanical energy would be lost in signal transmission through the hair. At frequencies of interest the hair would act stiff, thereby transmitting the stresses to the cantilever and the cantilever would act soft, thereby being very sensitive to the strain-induced piezoresistive transduction. If the frequencies were above the acceptable range, then the cantilever would act stiff, leading to an inefficient and reduced strain of the piezoresistive component. Although, such advanced band-pass designs may be challenging, nonetheless they serve to demonstrate the wide-range of design possibilities when using bioinspired design.

3.2. Anti-Biofouling Coatings for Sensors

The long-time presence of synthetic sensors in air or in fluid environments inevitably results in continuous adsorption of organic species; this is especially problematic in fluidic environment. Intense adsorption of large molecules (proteins, microorganisms), or biofouling, will eventually cause sensory systems to become inoperable. To prevent or hinder this phenomenon the artificial surfaces are usually coated with different, covalently grafted coatings with the ability to repel various species, provide gradient or responsive chemical composition, and alter the surface topology.^[76–79] Among the most popular coatings are mixed self-assembled monolayers, mixed brushes, and PEG brushes and

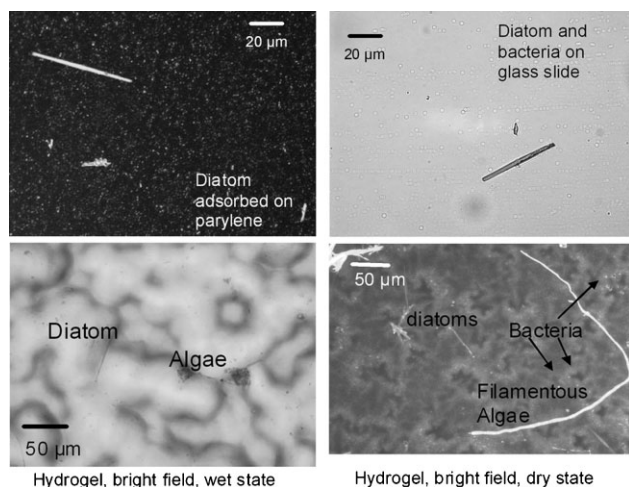


Figure 17. Optical images of parylene and glass slide (top) and thick PEG hydrogel film (bottom) after exposure to lake water.

molecular coatings, all explored in our previous studies.^[80–82] However, although these coatings can be successfully fabricated on planar, hydroxyl-terminated surfaces (glass, silicon, silica), the addition of robust anti-biofouling coatings on practical sensor devices with protective parylene coatings presents a special challenge and additional pretreatment as will be discussed below. It is worth noting that parylene-coated devices are covered with micro-organisms and diatoms within a few days of exposure after being placed into lake water (Fig. 17). Moreover, thick PEG hydrogel layers do not prevent intense biofouling to any great extent and thus more sophisticated PEG coatings are required.

The parylene-A coating is rich with reactive amine groups, which made further chemical modification of the surface possible with the assistance of several functional compounds presented in Scheme 1. In order to amplify the number of reactive amine groups, the devices were first dipped into a pentacrylate solution, followed by submersion in a tris(2-aminoethyl)amine solution. Next, the device was dipped into a glycidyl-methacrylate solution to create a surface rich with methacrylate groups. The sensor devices were then immersed in a dilute methoxy-PEG-monomethacrylate solution containing a type 1 photoinitiator, which was exposed to UV light to cure the monomer and form grafted PEG chains (Scheme 1, Fig. 18). Once polymerization was completed, the device was washed in a warm water bath to remove any unbound polymer and unreacted monomer. The resulting PEG coating was roughly 30–40 nm in height and lowered the water contact angle nearly 90% when compared to unreacted parylene-A. The initial smooth surface morphology is replaced with rougher nanoscale coating, as is evident from the AFM images (Fig. 18).

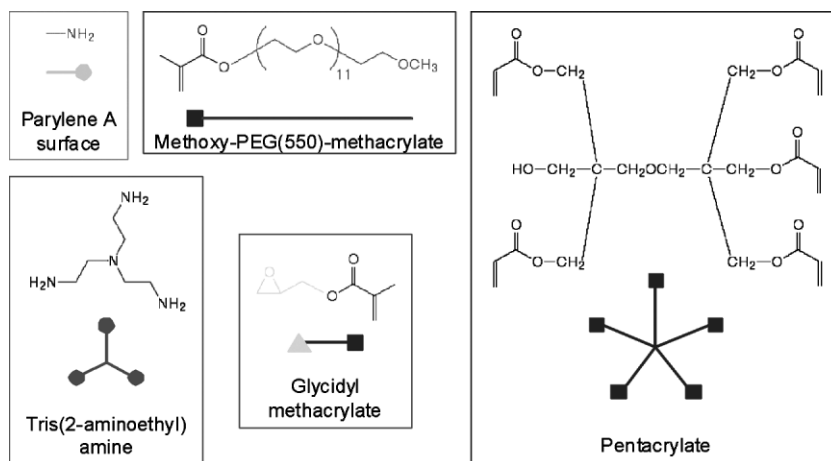
The advantages of this technique and the resulting coating are that it provides a highly effective antifouling surface that can be also patterned, can be made thicker or thinner by varying concentrations and UV exposure times, and creates a uniform, conformal layer around

all the crevices and hidden areas of the haircell, all after post-treatment of water-sensitive sensors with parylene coatings. A final benefit of this coating is that it is not only compatible with the PEG cupula previously mentioned, but it actually acts as an adhesion promoter for that chemistry.

The antifouling properties of these coatings can be verified using two techniques. In the first, 0.01 wt % of Alexa Fluor 594-labeled bovine serum albumin (BSA) in buffer was spotted on a parylene-A and a PEG-coated parylene-A test coupon for one minute. Afterwards, the samples were rinsed in water for one minute and imaged under a microscope (Fig. 19). It is evident that the BSA is tightly bound to the untreated surface yet is unable to adhere to the PEG surface. In the second experimental technique, the same two types of chips were incubated at 37 °C overnight, with shaking, in a culture of *Escherichia coli* that constitutively expressed green fluorescent protein (GFP). The samples were quickly rinsed in water before being imaged under the microscope. The GFP fluorescence of the bacteria is easily detected in the control sample, while noticeably absent on the PEG-coated sample, thus proving the efficiency of the anti-biofouling properties of coatings fabricated here (Fig. 19).

4. Infrared Imaging

Infrared imaging by biological species is another intriguing example which gives inspiration. Modern IR imaging with engineered detectors can generally be divided into two different categories: photon-based and thermal-based.^[83,84] Until relatively recently, most IR imaging development focused on photon sensors. Thermal-based detection, which involves transducing temperature, changes from the infrared absorption, was considered slow and insensitive. After decades of development, thermal-based detectors are being re-examined as an alternative to expensive photon detectors. After more recent developments, thermal-based IR detection has made a name for itself as a cheap and sensitive detector capable of TV-rate scanning speeds. Thermal-based detection includes a myriad of transduction techniques including bolometers and Golay cells, with sensitivities still usually below record values set by Nature.^[84]



Scheme 1. Selection of functionalized compounds for grafting of antibiofouling coating on parylene-coated sensors.

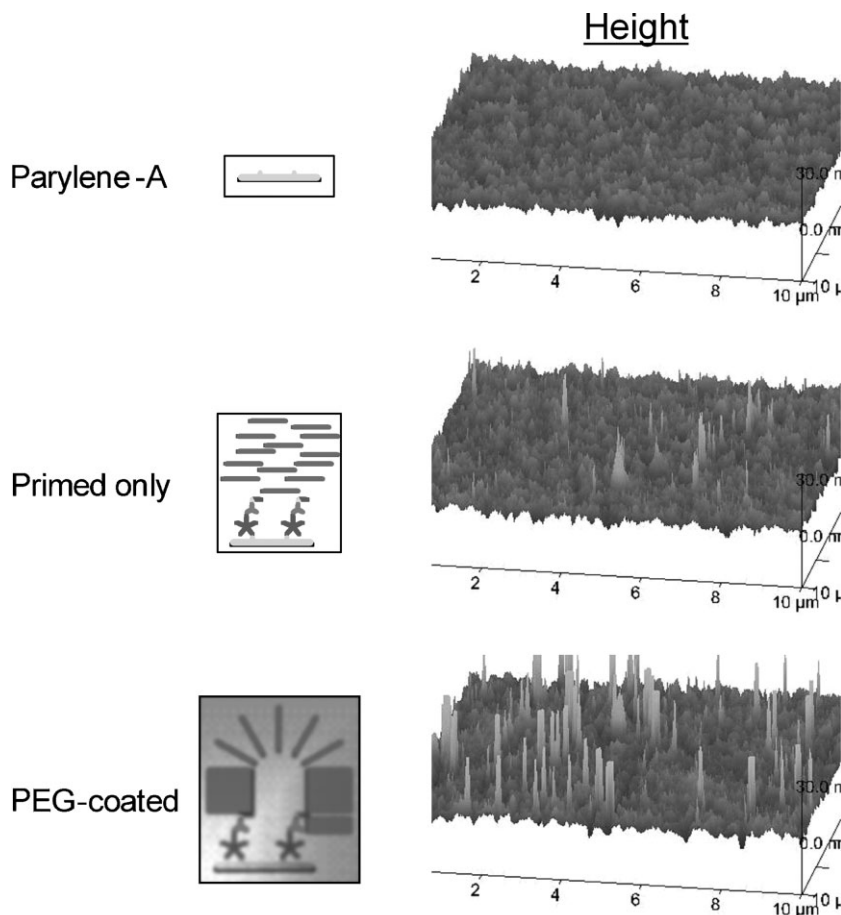


Figure 18. Step-by-step surface modification with PEG coatings and corresponding surface morphologies.

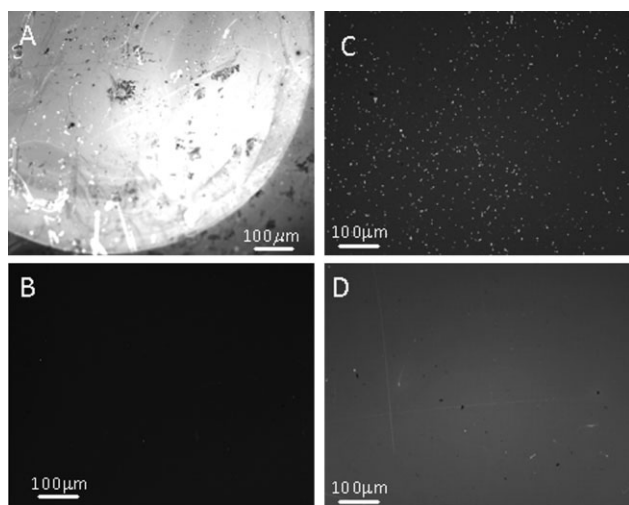


Figure 19. Comparison of the antifouling properties of bare parylene-A and PEG-coated samples. A) Return of fluorescently labeled BSA spotted onto the parylene-A after spotting for 1 minute and rinsing with water. B) Absence of fluorescence on a similarly spotted PEG-coated sample. C) Return of GFP-labeled *E. coli* growing on a bare parylene-A sample after incubating in LB media for 16 hours at 37 °C. D) The absence of growth of *E. coli* on a PEG-coated sample, prepared in a similar manner.

4.1. Infrared Sensing In Fire Beetles

To this end, here we consider one interesting example of thermal biological receptors. *Melanophila acuminata*, commonly called “fire beetles”, are attracted to forest fires from great distances, at least 0.5–3 miles (1 mile = 1.609 km) and maybe even up to 50–100 miles away.^[85–89] They mate and lay their eggs in freshly smoldering trees, which make a good environment for their larvae to develop. The beetles find these far-off fires by using IR pit organs located near where their middle legs meet their thorax (Fig. 20).^[91,92] Each organ is made up of about 75 spherical-shaped receptors. These spherical receptors are commonly broken into three main parts, an amorphous core, porous cuticular region, and an outer lamellae region (Fig. 20). The cuticular sphere is covered by a protoplasmic layer, which is roughly 300 nm thick, which is covered by a thin outer cuticle above the surface of the beetle. Supposedly, the sphere is freely suspended in a cavity within the cuticle stalk.

There is general agreement and good evidence that these IR receptors are thermal–mechanical based and are likely modified hair mechanoreceptors, much like trichobothria.^[93,94] Again, we see this approach of slightly modifying functional structures of receptors to transduce different stimuli. Their thermal–mechanical based transduction is in contrast to the directly thermal-based transduction employed in the IR receptors of snakes.^[95–97] Furthermore, it is agreed that the material making up the receptors absorbs IR radiation at a peak wavelength of about 3 μm that heats the receptor and through thermal expansion, the spherule volume increases and the dendritic tip is deformed, thereby sending off an action potential. That said, it is important to note that the transduction details are still unclear, specifically if the receptors operate via a thermal–pneumatic mechanism or through thermal expansion of the cuticular material. The receptors’ threshold stimulus is time dependent, but is quoted to be between 0.06–5 mW cm^{−2} and responding after 2 ms.^[98]

4.2. Bioinspired Infrared Sensing

Initially, the fire-beetle offered much motivation for our work, in that we knew thermal-mechanical transduction was promising and deserved further investigation. We started by developing ultrathin, flexible, freely suspended membranes, much like that the fire-beetle employs. Initially, our work focused on thermal–pneumatic transduction because thermal expansion transduction from a non-bimorph ultrathin film seemed unfeasible. It should be mentioned that previous work had demonstrated such a non-bimorph thermal-expansion based IR sensor, which was also

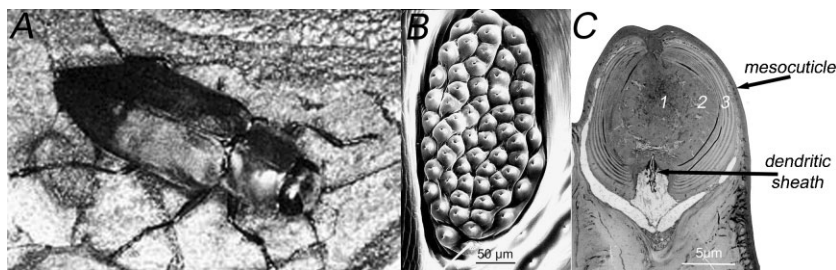


Figure 20. A) The Fire Beetle. B) An infrared pit organ composed of an array of micro-scale IR receptors. C) A cross-section of an infrared receptor. Adapted with permission from Reference [90]. Copyright 2004, Springer-Verlag.

inspired by the fire-beetle.^[90] The sensor was made from a Teflon disc (centimeter diameter) wedged against piezoelectric crystal; upon absorbing IR radiation the disc would expand and deform the crystal, thereby producing a voltage signal. Despite the impressive capabilities of this bioinspired sensor, it seemed impractical to scale this design to a microscale multipixel imager.

As will be discussed, after the thermal–pneumatic transduction work, we developed a new bioinspired non-bimorph thermal-expansion transduction that can be scaled down to very small sizes. Furthermore, by exploring both possible mechanisms employed by the fire-beetle, we were able to develop sensors with impressive properties and this engineering work may prove useful in further biological investigations of this creature.

4.2.1. Thermal–Pneumatic IR-Imagers

The thermal–pneumatic transduction mechanism is implemented by covering a cavity with an ultrathin film.^[99] As this covered cavity is exposed to IR radiation the enclosed gas heats and expands, thereby deflecting the membrane capping the cavity (Fig. 21).

The relation between deflection in the center of the sensor and the applied pressure, which is a measure of the sensitivity, can be expressed through the following equation:^[100–103]

$$P = P_0 + \left[C_0 \frac{Eh^4}{(1-\nu^2)r^4} + C_1 \frac{\sigma_0 h^2}{r^2} \right] \left(\frac{d}{h} \right) + C_2 \frac{Eh^4}{(1-\nu^2)r^4} \left(\frac{d}{h} \right)^3 \quad (1)$$

where P is the applied pressure, P_0 is the initial pressure, E is the elastic modulus, d is the deflection of the center of the membrane, ν is the Poisson's ratio, σ_0 is the residual stress, h is the film thickness, C 's are constants related to the film geometry (tabulated in the literature), and r is the length associated with the lateral dimensions, in this case the membrane radius.

At relatively large deflections, on the order of the film thickness, where the sensitivity, s , depends on the radius and thickness with the following relation

$$s \propto \frac{r^4}{h} \quad (2)$$

Therefore, in order to ensure high sensitivity, the sensors must be quite large. Often, they are on the millimeter-scale or larger. This constraint makes the feasibility of realizing multipixel imagers from thermal–pneumatics somewhat questionable. On the other hand, as previously discussed, there is good evidence that biology efficiently uses the thermal–pneumatic principle in a very small package.

Fire-beetles, with their highly sensitive miniature receptors, provided motivation to take a second look at miniaturized pneumatic IR transduction. In order to fabricate an array of sensitive Golay cells with a micrometer-scale footprint, we concentrated on minimizing the

thickness of the covering membrane. Ultrathin polymeric membranes were fabricated via layer-by-layer assembly, which allows excellent control over the thickness and the modulus of the film.^[104] A good balance between flexibility, robustness, and

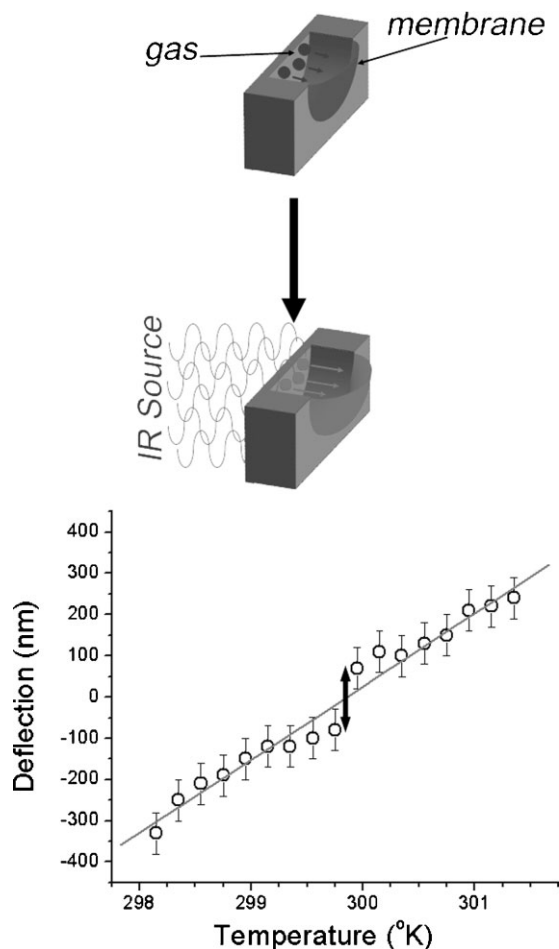


Figure 21. Thermal-pneumatic IR sensing Top: schematic explaining thermal-pneumatically driven membrane deflection. Bottom: membrane deflection versus temperature, note the nonlinearity at zero deflection. Reproduced with permission from Reference [106]. Copyright the American Chemical Society 2006.

reflectivity was obtained with films about 50 nm thick, with a gold nanoparticle layer serving as reflective and reinforcing filler.

We demonstrated that the ultrathin films have negligible gas permeability, thus serving as flexible sealers.^[105] Furthermore, the composite films have an elastic modulus of several GPa and tensile residual stress on the order of 10 MPa, which occurs during the drying process.^[103] It is also important to note that, under large stresses, these films show viscoelastic behavior. The films will reversibly creep, with the strain recovery times exceeding seconds, which is not surprising considering they are composed of an ionic-bound network. To fabricate the thermal–pneumatic imagers these membranes were deposited over microfabricated arrays (64 × 64, 4096 pixels) of 80 μm diameter, 100 μm deep cavities with 15 μm open channels separating each cavity to prevent cross-talk.^[106]

Measurements of membrane deflection with temperature were performed with interferometry in order to characterize the sensitivity of the individual sensors. The overall sensor response was found to be linear for several degrees above and below room temperature, but with a non-linearity occurring at room temperature (Fig. 21). This nonlinearity occurred at room temperature over a 200 mK temperature change with an overall membrane deflection of 200 nm and is expected from the first and second terms of Equation 1, when the deflection is on the order of thickness (Fig. 21). The overall sensitivity of the sensor was measured to be 0.12 nm mK⁻¹ near room temperature, except at the transition region, where it reached 1 nm mK⁻¹. This is vastly more sensitive than conventional microfabricated sensors based on inorganic membranes.^[107] Furthermore, the sensors demonstrated response times as fast as 60 ms, which is much faster than usual membrane or microcantilever sensors.^[108]

4.2.2. Polymeric Thermal-Buckling-Based Sensor Arrays

During the thermal–pneumatic work, it was observed that upon cooling the membranes below a critical temperature, wormlike buckling appeared in the open trenches (Fig. 22). These trenches do not undergo thermal–pneumatic deformation because of their

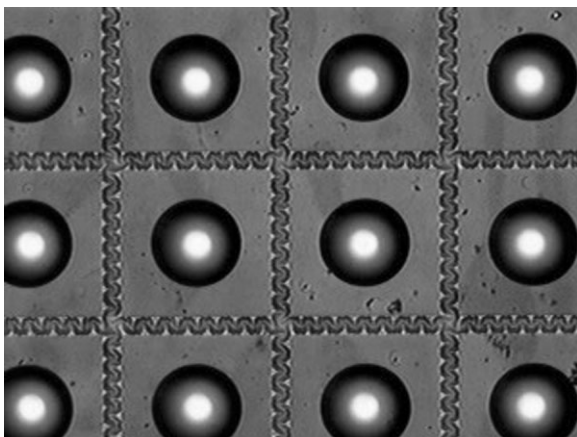


Figure 22. An optical image of a cooled sensor array. Note the wormlike buckling in the trenches and the high contrast of the sealed thermal–pneumatic sensors, which is caused by out of plane buckling. Reproduced with permission from Reference [106]. Copyright the American Chemical Society 2006.

open nature, and therefore were not expected to be affected by temperature changes. The buckling is the result of large thermally induced changes in the residual stress of the membranes. These wormlike buckling instabilities may be attributed, at least partially, to entropic negative thermal expansion, which is seen in polymers with anisotropic strain, such as crosslinked polymers and aligned fibers.^[109–111] As mentioned, these membranes have significant extensional residual stress, on the order of 10 MPa, which could lead to stretching of the polymer material in the film, thereby leading to entropic negative thermal expansion.^[100,109]

Buckling behavior of elastic materials has attracted attention in recent years.^[112–114] Several papers have explored out-of-plane buckling as a prospective sensing mechanism.^[115–119] It should also be mentioned that theoretical studies have recognized buckling as a possible sensing mechanism that is incredibly sensitive, but has a very small sensing range due to the discrete nature of buckling.^[115,116] Sensitivity could be an order of magnitude higher than that of conventional linear transduction, such as microcantilevers, with micrometer deflections over incredibly small ranges.^[115] Much of the enhanced response can be attributed to stress that builds prior to the critical buckling point, which acts to amplify the response. In fact, it is suggested that such huge deflections could likely be transduced optically, thereby eliminating the need for expensive photodetector-based methods.^[115] But a major issue regarding this approach is to keep the residual strain levels in this critical sensitivity region.

Implementing this transduction mechanism for IR sensing requires adjusting the residual stress to critical conditions by cooling the membrane below the critical buckling temperature. Then, when the membrane is exposed to incoming IR radiation, it will unbuckle. As mentioned, the open trenches, which are not thermal–pneumatic, had a buckling response after the IR imager chip was cooled below a certain critical temperature and a strong correlation was found between the large optical responses of the thermal–pneumatic detectors and the trench buckling. Upon further investigations, a unique feature was observed in interferometry data taken over a relatively large temperature range with the sensors displaying a nonsymmetric behavior, which is not predicted by equation 1 (Fig. 23).

This behavior led to huge sensitivities at modestly low temperatures. The sensitivity around 295 K would be expected to be roughly 28 nm K⁻¹, but in actuality it was measured to be 356 nm K⁻¹. These large deformations can be explained as out-of-plane buckling, which arises from thermally induced changes in residual stress. The disparity between the out-of-plane buckling of the sealed cavities and the in-plane buckling of the trenches can be explained as pneumatically guided buckling. This behavior is logical, considering that the pressure will provide some initial out-of-plane deformation, which will cause the out-of-plane buckling to become energetically favorable over in-plane buckling.

The viscoelastic creep of these films caused static measurements of the buckling transduction performance to be unstable, including diminished buckling with time and changes in critical buckling temperatures. To avoid the viscoelastic problems associated with the huge strains of buckling, the membranes should be operated in a dynamic mode. This was accomplished by cooling the membranes with a temperature-controlled thermoelectric cooler, while exposing them to chopped infrared laser light (Fig. 24).

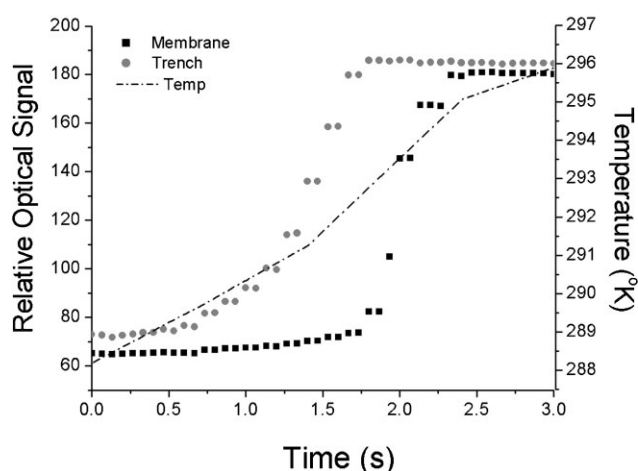
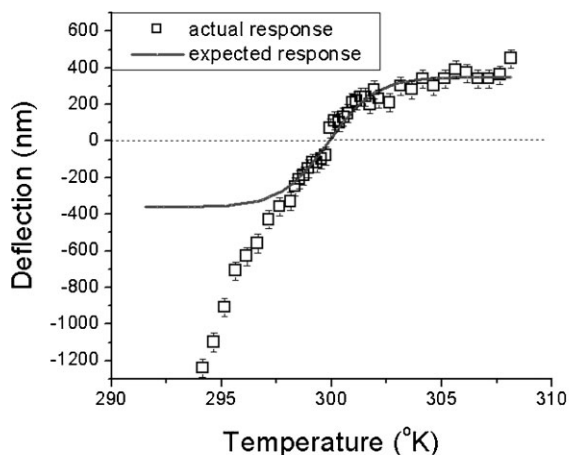


Figure 23. Relatively large scale interferometer results, black squares. Notice the nonsymmetric behavior around the zero point. The blue line indicates the theoretical behavior of thermal-pneumatic sensors. This huge increase in the sensitivity below room temperature indicates the onset of out-of-plane buckling. Bottom: a plot showing the similarity of the optical response of the pneumatic membrane and the worm-like buckling in channels.

Under this dynamic regime, the buckling proved to be very stable. As mentioned, major issues in implementing buckling-based sensing are tailoring the residual stress to be near the critical buckling threshold and the small sensing ranges associated with the discrete behavior of buckling.^[115] We solve these problems by controlling the residual stress with our approach. Furthermore, the response times were extremely fast (Fig. 25). At 10.3 Hz, a little over three frames per cycle, were recorded a clear sinusoidal signal that can be seen overlapping the primary sinusoidal signal, which occurs from temporal-aliasing caused by the sensor frequency being a noninteger multiple of the sampling frequency of the camera. Therefore, the fidelity of the intermediate stages of post-buckling deformation are captured in the data, indicating the relatively high quality of the optical transduction method. We were able to measure response times of 25 ms, by using the temporal aliasing signal.

In order to investigate the performance of the IR sensors, they were exposed to IR light with a relatively slow frequency (0.56 Hz) and the thermo-electric cooler temperature was changed, thereby

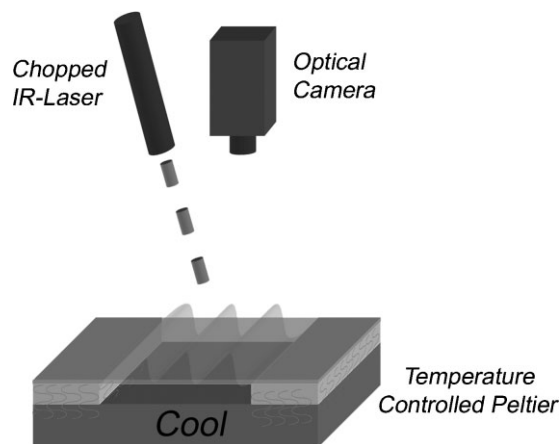


Figure 24. A schematic showing the experimental apparatus used to obtain and characterize the dynamic buckling-based IR sensors. This approach allows the residual stress to be modulated, which ensures the sensor can be kept in the highly sensitive buckling regime. Furthermore, it prevents viscoelastic creep of the LbL membranes caused by the large deformations.

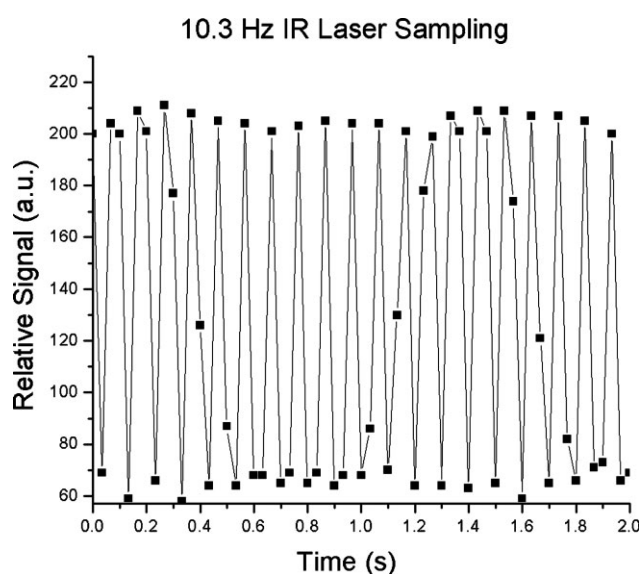


Figure 25. A plot of the relative optical amplitude versus time operated under a laser frequency of 10 Hz. Note the sinusoidal time aliasing caused by a difference between the optical camera sampling frequency and buckling frequency.

providing a measurable thermal signal. In this case the sensors were operated so that the laser power was relatively high and essentially saturated the unbuckling response and cooled enough to ensure the buckling deformation, thereby allowing the sensor to be sensitive in the region of the thermal cycle after the onset of buckling. Upon raising the temperature by 500 mK, from 17.00 °C to 17.50 °C, a significant damping in the optical signal was observed, specifically in the bottom part of the cyclic data corresponding to the buckling response (Fig. 26). Furthermore, the saturated unbuckling part of the thermal cycle was unaffected. The damping response is expected with heating and was shown to

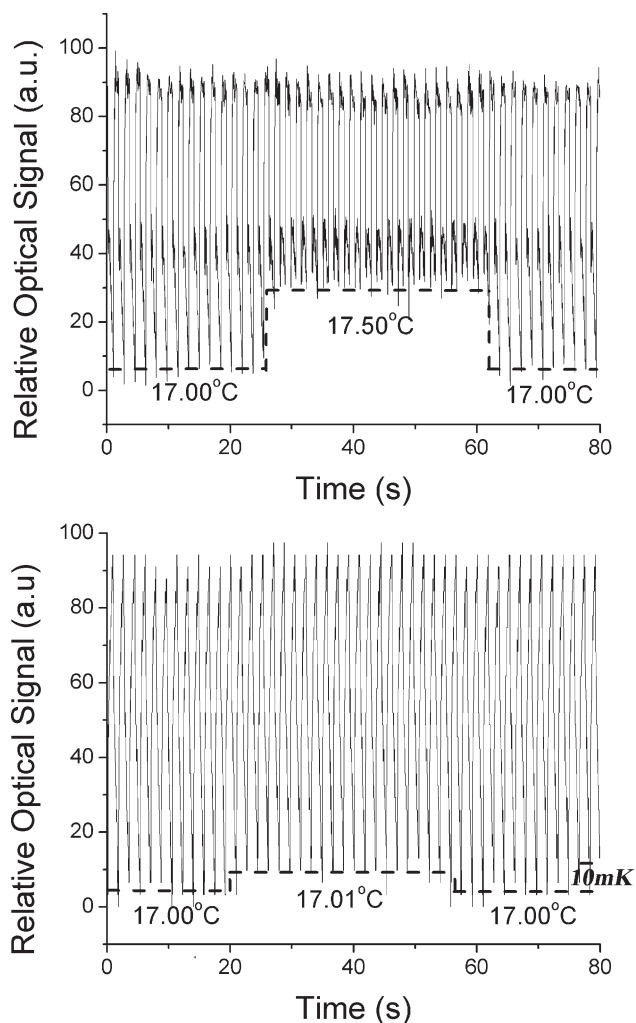


Figure 26. Top: a plot of relative optical signal versus time. The temperature was raised by 500 mK and then decreased. A dotted line at the bottom of the graph conveys the significant change in the amplitude due to the temperature change. Bottom: a plot of relative optical signal versus time. The temperature was raised by 10 mK and then returned. A dotted line at the bottom of the graph conveys the small, but noticeable change in amplitude due to the incredibly small temperature change.

be quite repeatable. This damped response is induced because the Peltier temperature increase causes it to act as a less efficient heat sink, which offsets the minimum temperature of the thermal cycle. The unbuckling is unaffected because the relatively high laser power already unbuckles the membrane out of the sensitive region.

In order to better demonstrate the extremely sensitive nature of the thermal buckling sensors, the temperature difference was reduced to 10 mK. Upon changing the temperature from 17.00 °C to 17.01 °C, a noticeable damping in the optical oscillation signal was observed again in the lower part of the thermal cycle (Fig. 26). The ability to resolve a 10mK difference is quite impressive considering that most thermal IR sensors have noise-equivalent temperature differences well exceeding 100 mK. Even more impressive is that such sensitivity was obtained with sensors with such extremely small foot-prints of 15 μm ; which is about two

orders of magnitude smaller than traditional membrane-based sensors.

Looking back to the fire-beetles, the controversy regarding their signal transduction details is not surprising, especially considering that we started with thermal–pneumatic based sensing and found an overlapping thermal-expansion based mechanism. In fact, these results sparked the possibility that fire-beetles in fact use both mechanisms simultaneously. Nonetheless, our exploration of these two different material-based transduction mechanisms, spurred by past biological research, serves as yet another example of the importance of both biologists and engineers in exploring biological ingenuity and implementing bioinspired design. In doing so, we successfully demonstrated a new infrared sensing mechanism that proved to be highly sensitive, fast and capable of performing in a very small footprint.

5. Conclusions

Bioinspired design approach is gaining momentum because of limitless wealth of novel approaches, especially with regard to materials. This article presents our current efforts in the area of bioinspired approaches to applying structured soft materials to sensing applications. Specifically, the article focused on fish-inspired structures for enhancing underwater flow sensing, spider-inspired structures for enhancing air-flow sensors, and beetle-inspired infrared transduction methods. By studying fish and understanding that the hydrogel-like cupula is a specialized structure that tailored the hair-cell for flow based sensing, we were able to take a fruitful bioinspired approach for developing our own engineered cupula. Furthermore, by studying blind cave fish cupula we were able to replicate the material and shape of the fish cupula, which led to dramatically enhanced flow sensing and allowed the engineered sensors' capabilities to rival that of the fish.

Through studying spiders that are highly dependent on vibrations and air-flow, we were able to elucidate a material-based mechanical signal filtering mechanism. Furthermore, we developed a spider-inspired two-tier hair that has significantly enhanced the durability of the sensors and provided the ground-work for developing air-flow sensors capable of material-based signal filtering. The sensing abilities of fire beetles provided motivation to improve thermal-pneumatic based sensors by using ultra-thin polymeric films. Work with the IR-sensing films naturally evolved into an exploration of thermal-stress induced buckling. The work with the thermal-pneumatic and thermal-buckling transduction paralleled questions regarding the details of the fire-beetle's IR transduction. From this article, the synergistic relationship of understanding the novel approaches of biology and applying those approaches to engineered systems should be quite evident. Furthermore, this article demonstrated that dramatic improvements to engineered systems are accessible through understanding and utilizing relatively simple lessons offered by biology in the application of functional materials.

Acknowledgements

The authors would like to thank the following people: Dr. S. Peleshanko, Dr. M. Ornatska, Dr. M. Julian, Mr. D. Lu, Prof. C. Jiang, Dr. M. Lemieux, Dr. S. Singamaneni, Prof. F. Barth, Mr. C. Schaber, Prof. S. Coombs,

Prof. J.A.C. Humphrey, Mr. W.C. Eberhardt, Prof. C. Liu, Dr. N. Chen, Mr. A. Hu, Dr. C. Tucker, Dr. Y. Yang, Prof. D. H. Reneker, Dr. T. Han, whose participation made this work possible. This work is supported by DARPA, AFOSR, AFRL, and NSF.

Received: April 6, 2009
Published online: July 24, 2009

- [1] Y. Bar-Cohen, in *Biomimetics: Biologically Inspired Technologies*, CRC Press, Boca Raton, FL **2006**, pp. 2–40.
- [2] T. Galante, J. Frank, J. Bernard, W. Chen, G. A. Lesieutre, G. H. Koopmann, *J. Intel. Mater. Syst. Struct.* **1999**, *10*, 962.
- [3] J. Hazel, M. Stone, M. S. Grace, V. V. Tsukruk, *J. Biomech.* **1999**, *32*, 477.
- [4] L. Mahadevan, S. Daniel, M. K. Chaudhury, *Proc. Natl. Acad. Sci. USA* **2004**, *101*, 23.
- [5] A. Woesz, J. C. Weaver, M. Kazanci, Y. Dauphin, D. E. Morse, J. Aizenberg, P. Fratzl, *J. Mater. Res.* **2006**, *21*, 2068.
- [6] J. C. Weaver, J. Aizenberg, G. E. Fantner, D. Kisailus, A. Woesz, P. Allen, K. Fields, M. J. Porter, F. W. Zok, P. K. Hansma, P. Fratzl, D. E. Morse, *J. Struct. Biol.* **2007**, *158*, 93.
- [7] J. Aizenberg, *Adv. Mater.* **2004**, *16*, 1295.
- [8] K. Autumn, Y. A. Liang, S. T. Hsieh, W. Zesch, W. P. Chan, T. W. Kenny, R. Fearing, R. J. Full, *Nature* **2000**, *405*, 681.
- [9] A. K. Geim, S. V. Dubonos, I. V. Grigorievam, K. S. Novoselov, A. A. Zhukov, S. Y. Shapoval, *Nat. Mater.* **2003**, *2*, 461.
- [10] K. Autumn, M. Sitti, Y. A. Liang, A. M. Peattie, W. R. Hansen, S. Sponberg, T. W. Kenny, R. Fearing, J. N. Israelachvili, R. J. Full, *Proc. Natl. Acad. Sci. USA* **2002**, *99*, 12252.
- [11] S. Yang, J. Aizenberg, *Nano Today* **2005**, *12*, 40.
- [12] S. Yang, G. Chen, M. Megens, C. K. Ullal, Y.-J. Han, R. Rapaport, E. L. Thomas, J. Aizenberg, *Adv. Mater.* **2005**, *17*, 435.
- [13] H. Lee, Y. Lee, A. R. Statz, J. Rho, T. G. Park, P. B. Messersmith, *Adv. Mater.* **2008**, *20*, 1619.
- [14] H. Lee, S. M. Dellatore, W. M. Miller, P. B. Messersmith, *Science* **2007**, *318*, 426.
- [15] N. T. Nguyen, *Flow Meas. Instrum.* **1997**, *8*, 7.
- [16] R. Darby, *Chemical Engineering Fluid Dynamics*, 2nd ed., Marcel Dekker, New York **2001**.
- [17] I. F. Akyildiz, D. Pompili, T. Melodia, *Ad Hoc Networks* **2005**, *3*, 257.
- [18] Y. Yang, J. Chen, J. Engel, S. Pandya, N. Chen, C. Tucker, S. Coombs, D. L. Jones, C. Liu, *Proc. Natl. Acad. Sci. USA* **2006**, *103*, 18891.
- [19] B. R. Clayton, B. S. Massey, *J. Sci. Instrum.* **1967**, *44*, 2.
- [20] P. Freymuth, *J. Sci. Instrum.* **1993**, *64*, 1.
- [21] Y. Yang, N. Chen, C. Tucker, J. Engel, S. Pandya, C. Liu, presented at the MEMS 2007 20th IEEE Int. Conf. on Micro Electro Mechanical Systems, Kobe, Japan, January **2007**.
- [22] J. Engel, J. Chen, C. Liu, D. Bullen, *IEEE/ASME J. Microelectromech. Syst.* **2006**, *15*, 729.
- [23] N. Chen, C. Tucker, J. M. Engel, Y. Yang, S. Pandya, C. Liu, *J. Microelectromech. Syst.* **2007**, *16*, 999.
- [24] Z. Fan, J. Chen, J. Zou, D. Bullen, C. Liu, F. Delcomyn, *J. Microelectromech. Syst.* **2002**, *12*, 655.
- [25] A. B. A. Kroese, J. M. Van der Zalm, J. Van der Berken, *Pflug. Arch. Eur. J. Phys.* **1978**, *375*, 167.
- [26] S. Coombs, J. Janssen, in: *The Mechanosensory Lateral Line: Neurobiology and Evolution*, (Eds: S. Coombs, P. Görner, H. Münz), Springer, New York **1989**, pp. 299–319.
- [27] S. Coombs, S. M. van Netten, *Fish Physiol.* **2006**, *23*, 103.
- [28] H. Bleckmann, J. Mogdans, G. Dehnhardt, in: *Ecology of Sensing*, (Eds: F. G. Barth, A. Schmid), Springer, New York **2001**, pp. 149–168.
- [29] M. J. McHenry, S. M. van Netten, *J. Exp. Biol.* **2007**, *210*, 4244.
- [30] E. J. Denton, J. Gray, *Proc. R. Soc. London Ser. B* **1983**, *218*, 1.
- [31] A. B. A. Kroese, N. A. M. Schellart, *J. Neurophysiol.* **1992**, *68*, 2212.
- [32] S. M. Van Netten, A. B. A. Kroese, in: *The Mechanosensory Lateral Line: Neurobiology and Evolution*, (Eds: S. Coombs, P. Görner, H. Münz), Springer, New York **1989**, pp. 247–263.
- [33] A. Flock, A. J. Duvall, *J. Cell Biol.* **1965**, *25*, 1.
- [34] E. Perozo, A. Kloda, D. M. Cortes, B. Martinac, *Nat. Struct. Biol.* **2002**, *9*, 696.
- [35] A. Assad, D. P. Corey, *J. Neurosci.* **1992**, *12*, 3291.
- [36] J. Howard, W. M. Roberts, A. J. Hudspeth, *Annu. Rev. Biophys. Biophys. Chem.* **1988**, *17*, 99.
- [37] R. Fettiplace, P. A. Fuchs, *Annu. Rev. Physiol.* **1999**, *61*, 809.
- [38] L. G. Tilney, M. S. Tilney, D. J. DeRosier, *Annu. Rev. Cell Biol.* **1992**, *8*, 257.
- [39] R. A. Eatock, *Annu. Rev. Neurosci.* **2000**, *23*, 285.
- [40] J. T. Corwin, M. E. Warchol, *Annu. Rev. Neurosci.* **1991**, *14*, 301.
- [41] V. S. Markin, A. J. Hudspeth, *Annu. Rev. Biophys. Biomol. Struct.* **1995**, *24*, 59.
- [42] T. Teyke, *Brain Behav. Evolut.* **1990**, *35*, 23.
- [43] M. J. McHenry, J. A. Strother, S. M. van Netten, *J. Comp. Physiol. A* **2008**, *194*, 795.
- [44] M. Denny, *J. Comp. Neurol.* **1937**, *68*, 39.
- [45] J. P. Kelly, S. M. Van Netten, *J. Morphol.* **1991**, *207*, 23.
- [46] S. A. Chizhik, Z. Huang, V. V. Gorbunov, N. K. Myshkin, V. V. Tsukruk, *Langmuir* **1998**, *14*, 2606.
- [47] V. V. Tsukruk, Z. Huang, *Polymer* **2000**, *41*, 5541.
- [48] V. V. Tsukruk, A. Sidorenko, V. V. Gorbunov, S. A. Chizhik, *Langmuir* **2001**, *17*, 6715.
- [49] V. V. Tsukruk, V. V. Gorbunov, Z. Huang, S. A. Chizhik, *Polym. Int.* **2000**, *49*, 441.
- [50] V. V. Tsukruk, Z. Huang, S. A. Chizhik, V. V. Gorbunov, *J. Mater. Sci.* **1998**, *33*, 4905.
- [51] S. Peleshanko, M. D. Julian, M. Ornatka, M. E. McConney, M. C. LeMieux, N. Chen, C. Tucker, Y. Yang, C. Liu, J. A. C. Humphrey, V. V. Tsukruk, *Adv. Mater.* **2007**, *19*, 2903.
- [52] A. Revzin, R. Russell, V. K. Yadavalli, W.-G. Koh, C. Deister, D. D. Hile, M. B. Mellott, M. V. Pishko, *Langmuir* **2001**, *17*, 5440.
- [53] K. D. Anderson, D. Lu, M. E. McConney, T. Han, D. H. Reneker, V. V. Tsukruk, *Polymer* **2008**, *49*, 5284.
- [54] L. D. Landau, E. M. Lifshitz, *Fluid Mechanics*, Pergamon, Oxford **1959**.
- [55] M. E. McConney, N. Chen, D. Lu, H. A. Hu, S. Coombs, C. Liu, V. V. Tsukruk, *Soft Matter* **2009**, *5*, 292.
- [56] P. Gerner, *Z. Vergl. Physiol.* **1963**, *47*, 316.
- [57] J. Doshi, D. H. Reneker, *J. Electrostat.* **1995**, *35*, 151.
- [58] D. H. Reneker, I. Chun, *Nanotechnology* **1996**, *7*, 216.
- [59] Z. M. Huang, Y. Z. Zhang, M. Kotaki, S. Ramakrishna, *Compos. Sci. Technol.* **2003**, *63*, 223.
- [60] D. Li, Y. Xia, *Adv. Mater.* **2004**, *16*, 1151.
- [61] D. H. Reneker, W. Kataphinan, A. Theron, E. Zussman, A. L. Yarin, *Polymer* **2002**, *43*, 6785.
- [62] T. Subbiah, G. S. Bhat, R. W. Tock, S. Parameswaran, S. S. Ramakumar, *J. Appl. Polym. Sci.* **2005**, *96*, 557.
- [63] J. M. Deitzel, J. D. Kleinmeyer, J. K. Hirvonen, N. C. Beck Tan, *Polymer* **2001**, *42*, 8163.
- [64] T. Steinmann, J. Casas, G. Krijnen, O. Dangles, *J. Exp. Biol.* **2006**, *209*, 4398.
- [65] C. Y. Lee, C. Y. Wen, H. H. Hou, R. J. Yang, C. H. Tsai, L. M. Fu, *Microfluid. Nanofluid.* **2009**, *6*, 363.
- [66] F. G. Barth, *A Spider's World: Senses and Behavior*, Springer, New York **2002**.
- [67] F. G. Barth, *Naturwissenschaften* **2000**, *87*, 51.
- [68] F. G. Barth, U. Wastl, J. A. C. Humphrey, R. Devarakonda, *Philos. Trans. R. Soc. London Ser. B* **1993**, *340*, 445.
- [69] F. G. Barth, *Zoology* **2002**, *105*, 271.
- [70] F. G. Barth, *Curr. Opin. Neurobiol.* **2004**, *14*, 415.
- [71] F. G. Barth, in *Sensors and Sensing: A Biologist's View, in Sensors and Sensing in Biology and Engineering*, (Eds: F. G. Barth, J. A. C. Humphrey, T. W. Secomb), Springer, New York **2003**, pp. 2–15.

- [72] J. A. C. Humphrey, F. G. Barth, in *Advances in Insect Physiology Insect Mechanics and Control*, Vol. 34 (Eds: S. J. Simpson), Elsevier, London, UK **2008**.
- [73] F. G. Barth, A. Höller, *Philos. Trans. R. Soc. London Ser. B* **1999**, 354, 183.
- [74] M. E. McConney, C. F. Schaber, M. D. Julian, F. G. Barth, V. V. Tsukruk, *J. R. Soc. Interface* **2007**, 4, 1135.
- [75] M. E. McConney, C. F. Schaber, M. D. Julian, W. C. Eberhardt, J. A. C. Humphrey, F. G. Barth, V. V. Tsukruk, *J. R. Soc., Interface* **2009**, 6, 681.
- [76] I. Luzinov, S. Minko, V. V. Tsukruk, *Soft Matter* **2008**, 4, 714.
- [77] B. D. Ratner, S. J. Bryant, *Annu. Rev. Biomed. Eng.* **2004**, 6, 41.
- [78] V. V. Tsukruk, *Adv. Mater.* **2001**, 13, 95.
- [79] I. Luzinov, S. Minko, V. V. Tsukruk, *Prog. Polym. Sci.* **2004**, 29, 635.
- [80] N. B. Sheller, S. Petrash, M. D. Foster, V. V. Tsukruk, *Langmuir* **1998**, 14, 4535.
- [81] D. Julthongpiput, Y.-H. Lin, J. Teng, E. R. Zubarev, V. V. Tsukruk, *J. Am. Chem. Soc.* **2003**, 125, 15912.
- [82] S. Peleshanko, J. Jeong, R. Gunawidjaja, V. V. Tsukruk, *Macromolecules* **2004**, 37, 6511.
- [83] A. Rogalski, *Prog. Quantum Electron.* **2003**, 27, 59.
- [84] A. Rogalski, *Infrared Detectors-Electrocomponent Science Monographs*, Vol. 10, Gordon and Breach, Amsterdam **2000**.
- [85] W. G. Evans, *Nature* **1964**, 202, 211.
- [86] W. G. Evans, *Ecology* **1966**, 47, 1061.
- [87] W. Gronenberg, H. Schmitz, *Cell Tissue Res.* **1999**, 297, 311.
- [88] D. X. Hammer, D. Dave, T. E. Milner, B. Choi, H. G. Rylander, A. J. Welch, *Comp. Biochem. Physiol. A* **2002**, 132, 381.
- [89] H. Schmitz, H. Bleckmann, *J. Comp. Physiol. A* **1998**, 182, 647.
- [90] H. Bleckmann, H. Schmitz, G. Von der Emde, *J. Comp. Physiol. A* **2004**, 190, 971.
- [91] H. Schmitz, H. Bleckmann, *Int. J. Insect Morphol. Embryol.* **1997**, 26, 205.
- [92] H. Schmitz, M. Murtz, H. Bleckmann, *J. Comp. Physiol. A* **2000**, 186, 543.
- [93] T. Vondran, K.-H. Apel, H. Schmitz, *Tissue Cell* **1995**, 27, 645.
- [94] J. Hazel, N. Fuchigami, V. Gorbunov, H. Schmitz, M. Stone, V. V. Tsukruk, *Biomacromolecules* **2001**, 2, 304.
- [95] A. L. Campbell, R. R. Naik, L. Sowards, M. O. Stone, *Micron* **2002**, 33, 211.
- [96] N. Fuchigami, J. Hazel, V. V. Gorbunov, M. Stone, M. Grace, V. V. Tsukruk, *Biomacromolecules* **2001**, 2, 757.
- [97] V. Gorbunov, N. Fuchigami, M. Stone, M. Grace, V. V. Tsukruk, *Biomacromolecules* **2002**, 3, 106.
- [98] D. X. Hammer, H. Schmitz, A. Schmitz, H. G. Rylander, III, A. J. Welch, *Comp. Biochem. Physiol. A* **2001**, 128, 805.
- [99] M. J. E. Golay, *Rev. Sci. Instrum.* **1947**, 18, 347.
- [100] S. Markutsya, C. Jiang, Y. Pikus, V. V. Tsukruk, *Adv. Funct. Mater.* **2005**, 15, 771.
- [101] C. Poilane, P. Delobelle, C. Lexcellent, S. Hayashi, H. Tobushi, *Thin Solid Films* **2000**, 370, 156.
- [102] S. Jayaraman, R. L. Edwards, K. J. Hemker, *J. Mater. Res.* **1999**, 14, 688.
- [103] R. Gunawidjaja, C. Jiang, S. Peleshanko, M. Ornatska, S. Singamaneni, V. V. Tsukruk, *Adv. Funct. Mater.* **2006**, 16, 2024.
- [104] C. Jiang, S. Markutsya, Y. Pikus, V. V. Tsukruk, *Nat. Mater.* **2004**, 3, 721.
- [105] C. Jiang, B. M. Rybak, S. Markutsya, P. E. Kladitis, V. V. Tsukruk, *Appl. Phys. Lett.* **2005**, 86, 121912.
- [106] C. Jiang, M. E. McConney, S. Singamaneni, E. Merrick, Y. Chen, J. Zhao, L. Zhang, V. V. Tsukruk, *Chem. Mater.* **2006**, 18, 2632.
- [107] K. Yamashita, A. Murata, M. Okuyama, *Sens. Actuators A* **1998**, 66, 29.
- [108] S. Singamaneni, M. C. LeMieux, H. P. Lang, C. Gerber, Y. Lam, S. Zauscher, P. G. Datskos, N. V. Lavrik, H. Jiang, R. R. Naik, T. J. Bunning, V. V. Tsukruk, *Adv. Mater.* **2008**, 20, 653.
- [109] H. M. James, E. Guth, *J. Chem. Phys.* **1943**, 11, 455.
- [110] R. H. Baughman, *J. Chem. Phys.* **1973**, 58, 2976.
- [111] S. Singamaneni, M. C. LeMieux, H. Jiang, T. J. Bunning, V. V. Tsukruk, *Chem. Mater.* **2007**, 19, 129.
- [112] N. Bowden, S. Brittain, A. G. Evans, J. W. Hutchinson, G. M. Whitesides, *Nature* **1998**, 393, 146.
- [113] C. Jiang, S. Singamaneni, E. Merrick, V. V. Tsukruk, *Nanolett.* **2006**, 6, 2254.
- [114] C. M. Stafford, C. Harrison, K. L. Beers, A. Karim, E. J. Amis, M. R. Vanlandingham, H. Kim, W. Volksen, R. D. Miller, E. E. Simonyi, *Nat. Mater.* **2004**, 3, 545.
- [115] M. R. Begley, M. Utz, U. Komaragiri, *J. Mech. Phys. Solids* **2005**, 53, 2119.
- [116] M. Utz, M. R. Begley, *J. Mech. Phys. Solids* **2008**, 56, 801.
- [117] M. R. Begley, N. S. Barker, *J. Micromech. Microeng.* **2007**, 17, 350.
- [118] M. R. Begley, M. Utz, *J. Appl. Mech.* **2008**, 75, 021008.
- [119] A. Ettouhami, A. Essaid, N. Ouakrim, L. Michel, M. Limouri, *Sens. Actuators A* **1996**, 57, 167.